2009

Study Of The Hydrodynamics Of Droplet Impingement On A Dry Surface Using Lattice Boltzmann Method

Xin Gu
University of Central Florida

STUDY OF THE HYDRODYNAMICS OF DROPLET IMPINGEMENT ON A DRY SURFACE USING LATTICE BOLTZMANN METHOD

by

XIN GU
B.S. China Agricultural University, 2006

A thesis submitted in partial fulfillment of the requirements
for the degree of Master of Science
in the Department of Mechanical, Materials and Aerospace Engineering
in the College of Engineering and Computer Science
at the University of Central Florida
Orlando, Florida

Spring Term
2009

ABSTRACT

In this work, a two-phase lattice Boltzmann method (LBM) approach is implemented to investigate the hydrodynamic behavior of a single droplet impingement on a dry surface. LBM is a recently developed powerful technique to compute a wide range of fluid flow problems, especially in applications involving interfacial dynamics and complex geometries. Instead of solving the non-linear Navier-Stokes equations, which are complicated partial differential equations, LBM solves a set of discretized linear equations, which are easy to implement and parallelize. The fundamental idea of LBM is to recover the macroscopic properties of the fluid which obeys Navier-Stokes equations, by using simplified kinetic equations that incorporate the essential physics at the microscopic level.

Considering the numerical instability induced by large density difference between two phases during the LBM simulations, the particular LBM scheme used in this study has its benefits when dealing with high density ratios. All the simulations are conducted for density ratio up to 50 in a three-dimensional Cartesian coordinate system, and three important dimensionless numbers, namely Weber number, Reynolds number and Ohnesorge number, are used for this study.

To validate this multiphase LBM approach, several benchmark tests are conducted. First, the angular frequency of an oscillating droplet is calculated and compared with the corresponding theoretical value. Errors are found to be within 6.1% for all the cases. Secondly, simulations of binary droplet collisions are conducted in the range of

20<We<80. Three different types of outcome, namely coalescence collision, separating collision and stretching collision, are presented. Then, the normal impact of a liquid drop impinging on a smooth dry surface is simulated at various liquid Weber and Reynolds numbers. A novel wall boundary condition is implemented in order to study the effects of wetting characteristic of the impinging surface. Results are shown to compare the spread factor dependence on impact velocity, liquid density, liquid viscosity, surface tension and surface wetting characteristics. The results are validated with experimental data. Two different outcomes are obtained: deposition and splashing break-up. The transition to splashing is found to be dependent on the liquid Weber and Reynolds numbers.

ACKNOWLEDGEMENTS

I would like to express my sincere gratitude to my advisor, Dr. Ranganathan Kumar, for providing me a lot freedom during the research and for his supervision of my thesis work. Without his support and guidance this work would not have been possible. He has always been encouraging when I meet difficulties and get frustrated.

I would like to thank Dr. Louis Chow and Dr. Saptarshi Basu for serving as my Thesis Committee members and providing valuable comments and suggestions for my research.

I would like to thank my labmate, Amit Gupta for helping me better understand the methodology, Lattice Boltzmann Method, when I started my research. He has been continuously providing useful discussions during my whole graduate career. I would like to thank Parveen Sachdeva for his help in the aspect of UNIX system operations and some coding issues. I would also like to express my gratitude towards my previous labmate, Navid Aminimanash, for his encouragement and help when I was first year here.

I would like to thank my parents, my father Xingzhi Gu, my mother Fengju Guo, for their endless love and support during my whole life.

I would also like to acknowledge UCF I2 Lab for providing the computing resources.

TABLE OF CONTENTS

LIST OF FIGURES

LIST OF TABLES

LIST OF ABBREVIATIONS

a,b,T = free parameter determining ϕ

B = impact parameter

$\boldsymbol{e_i}$ = particle velocity

D = diameter of the droplet

d = diameter of the liquid lamella

E_i, F_i, H_i = coefficients in equilibrium distribution functions

f_i = particle distribution function for an order parameter

f_i^{eq} = equilibrium particle distribution function for f_i

g_i = particle distribution function for predicted velocity $\mathbf{u}^*$

g_i^{eq} = equilibrium particle distribution function for g_i

h_i = particle distribution function for pressure

L_x, L_y, L_z = dimensions of the computational domain

Oh = Ohnesorge number

p = pressure

p_0 = Equation of state function determining ϕ

Re = Reynolds number

t = time in LBM unit

t^* = dimensionless time defined as tV/D

$\boldsymbol{u}$ = corrected velocity of a two-phase fluid

$\boldsymbol{u}^*$ = predicted velocity of a two-phase fluid

V = impact velocity

We = Weber number

X = vertical distance between the centers of the two droplets

$\delta_{\alpha\beta}$ = Kronecher delta

κ_f = constant parameter determining the width of interface

κ_g = constant parameter determining the strength of surface tension

μ = viscosity

ρ = density

σ = surface tension

τ_f = relaxation time for f_i

τ_g = relaxation time for g_i

τ_h = relaxation time for h_i

ϕ = order parameter to distinguish two phases

Ω_i = collision operator

ψ = bulk free energy density

ξ = direction normal to the interface

$\xi_{\max}$ = maximum spread factor

ε = convergence criteria

θ_w = Static contact angle

Ω = Wetting potential

η = Surface wetting force

CHAPTER ONE: INTRODUCTION

The droplet impingement on surfaces is an everyday occurrence which has several applications in fluid mechanics. Interactions between drops and surfaces are encountered both in nature and a wide range of science and engineering applications, such as rain drops falling on the ground, ink-jet printing, spray cooling of hot surfaces (turbine blades, lasers, semiconductor chips), spray painting and coating, plasma spraying, fuel spray atomization in combustion chambers of both gas turbines and internal combustion engines, industrial washing, and more recently in microfabrication and microchannels. Another very practical application is in metallurgy. Metals or alloys during their processing are usually liquids. This fact is used to study their properties by determining the surface tension of metals from the shape of a molten metal drop to understand reactions on the drop surface. At high impact velocity, the drop may splash, forming secondary drops. This is obviously undesirable in applications such as ink-jet printing and spray coating. However, splashing may be desirable in combustion chambers for instance. Thus, a fundamental understanding of fluid dynamics associated with droplet impingement on surfaces and their interactions with one another and then correctly predicting its subsequent outcome are very important to achieve the desired performance in those applications.

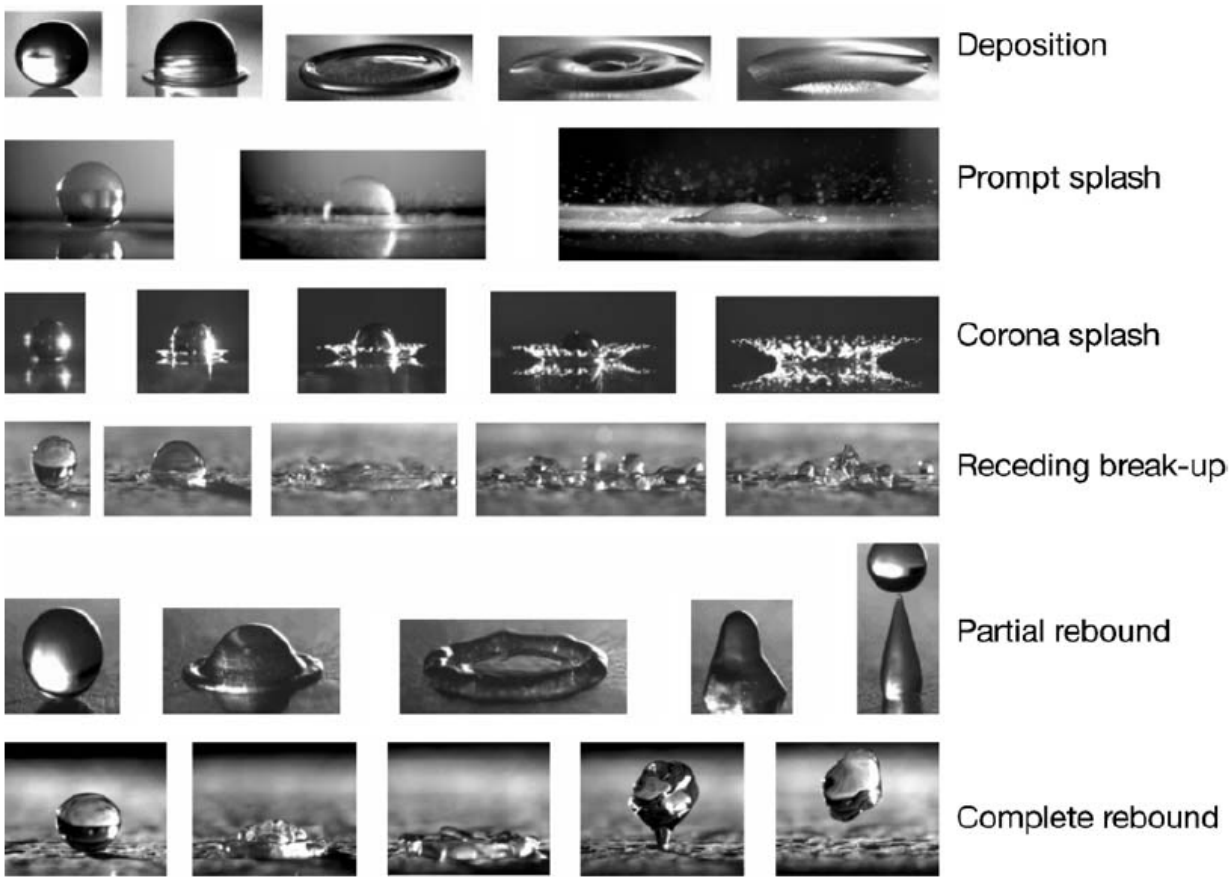

Figure 1: Six different outcomes of drop impact on a dry surface (From Rioboo et al. (2001))

When a droplet hits on a rigid dry surface, several outcomes may occur, and they may be broadly classified as deposition, splashing and rebounding. In a recent experimental study conducted by Riboo et al. (2001), six possible outcomes of drop impact on a dry wall were revealed, shown in Figure 1, namely deposition, prompt splash, corona splash, receding break-up, partial rebound and complete rebound. In their study, the droplet size, impact velocity, droplet viscosity, surface tension of the droplet, the surface roughness amplitude and the surface wettability characteristics were varied to examine their influence on the impingement outcomes. Thus, the physics of

droplet impingement is fairly complex. To systematically study the dynamics of a spreading droplet, three important dimensionless numbers are usually employed:

Weber number: $\mathrm{We}=\frac{\rho_{\mathrm{L}} V^2 D}{\sigma}$ (1.1)

Reynolds number: $\mathrm{Re}=\frac{\rho_{\mathrm{L}} V D}{\mu_L}$ (1.2)

Ohnesorge number: $Oh = \sqrt{We} / \mathrm{Re} = \mu_L / \sqrt{\rho_L D \sigma}$ (1.3)

where $\rho_{\mathrm{L}}, \mu_L, \sigma, D$ are the density, dynamic viscosity, surface tension and the diameter of the liquid droplet, respectively. V is the impact velocity. Ohnesorge number is a combination of Weber number and Reynolds number, and the importance of it is that it solely represents the properties of the liquid droplets, while Weber number represents the ratio of the droplet kinetic energy on impact to the surface tension energy, and Reynolds number represents the inertial force of the droplet to viscous force. Another important dimensionless parameter which is used to characterize the drop/surface interactions is the spread factor, defined as the ratio of the spreading film diameter to the initial spherical droplet diameter:

$$d^* = d / D \tag{1.4}$$

Studies of droplet impingement on dry surface have been mostly experimental so far. However, as argued by Mukherjee (2006), experimental investigations are not adequate enough to clarify the controlling physics because the impingement process occurs at vastly different length and time scales. For example, surface tension forces may act over the length scales only of the order of several molecular mean free paths while fluid flow scales may be of the order of the drop

diameter. Scales ranging from microscopic to macroscopic may be involved. Thus, multi-scale modeling is needed for computational studies. The relevant traditional computational fluid dynamics methods will be reviewed in next chapter.

The numerical simulation of multiphase flows is a very challenging class of problems because of the inherent difficulty in tracking the fluid interfaces, mass conservation and correct treatment of the surface tension force. In recent years, the lattice Boltzmann method (LBM) has emerged as a very promising numerical approach for simulation of complex and multiphase flows. The success of LBM based simulations is mainly due to their mesoscopic and kinetic nature, which enables the simulation of macroscopic interfacial dynamics with the underlying microscopic nature.

In this thesis, the lattice Boltzmann method is employed to study the droplet impingement on a dry surface in a three-dimensional Cartesian coordinate system. The thesis consists of six chapters, and it is organized as follows. In chapter 2, the literature review of both experimental studies and traditional computational fluid dynamics (CFD) methods on droplet impingement is presented, and various LBM schemes for multiphase flow are discussed and compared. In chapter 3, a brief history of LBM developed from lattice gas automata (LGA) is reviewed, and the mathematical derivations of lattice Boltzmann equation (LBE) from continuum Boltzmann equation, Navier-Stokes from LBE are presented. Single phase fluid flow simulation, e.g., Poiseuille flow, is presented as a benchmark test. Two different kinds of wall boundary conditions are implemented and the results are compared. In chapter 4, the multiphase lattice

Boltzmann scheme employed in this study is presented, and its algorithm is discussed. Capillary wave and binary drop collision are simulated as benchmark tests to validate the LBM scheme. In chapter 5, simulations of a droplet impingement on a dry surface are presented under a variety of different Weber numbers, Reynolds numbers and Ohnesorge numbers. Deposition, splashing and rebound are investigated as different outcomes of the impingement. The transition for the impingement outcome from deposition to splashing is qualitatively studied by a simple energy conservation analysis. In chapter 6, conclusions of this study are presented.

CHAPTER TWO: LITERATURE REVIEW

In one of the earliest studies of drop-surface interactions, Worthington (1876) reported his experimental observations of drops of milk and mercury impacting on glass. Other notable earlier works were done by Engel (1955), Ford et al. (1967). However, most significant studies of droplet impingement have been done in the last two decades using high-speed photographic techniques. There are three main types of investigations in this field: experimental, computational simulation and theoretical calculations. They will be discussed in this chapter.

2.1 Experimental studies of drop-wall interactions

Experimental studies have been done mostly by using imaging capture systems. Some of the most important experimental studies are briefly discussed in this section, and the primary experimental data of all those studies are summarized in Table 1.

Engel (1955) conducted one of the first studies that utilized a high-speed camera to photograph the impingement process. His work verified some of the observations made by Worthington (1876). Ford & Furmidge (1967) contributed to the understanding of the impingement process by dividing it into several stages (initial spreading, retraction, secondary spreading). The importance of viscosity, kinetic energy and surface energy were also discussed. In 1990s, several droplet impingement studies were conducted using improved camera techniques. Chandra & Avedisian (1991) employed a single shot photographic technique with a laser triggering system to study the

effect of surface temperature on spreading. Scheller & Bousfield (1995) used a video recording system to study the effect of viscosity on the impingement process.

Table 1: Summary of the parameters from important experiments on droplet impingement on dry surface (From Ok (2005))

Authors (Year)	Liquids	Surfaces	V (m/s)	d (mm)	μ (cP)	σ (mN/m)	Re	We	d^*_{max}
Worthington (1876)	Milk, Mercury	Smoked and unsmoked glass	1, 1.4, 1.7 2.0, 2,2	6.0 and 4.1	N/A	N/A	N/A	N/A	N/A
Engel (1955)	Water, surfactant solution	glass and filter paper	3 and 11	N/A	N/A	N/A	N/A	N/A	N/A
Ford et al. (1967)	Water, surfactant solution	beeswax, cellulose acetate glass	2.6-4.3	0.62, 0.78, 0.89, 1.1	1	72.8, other	1600-4496	57-256	2.65-4.40
Tsurutani et al. (1990)	Fluorescent dye solution	glass	~3.1	5.2	1	60	16300	1020	5.5
Chandra et al. (1991)	n-heptane	stainless steel surface, ceramic	0.93	1.5	0.42	20.8	2300	43	4.0
Asai et al. (1993)	3 water-based ink	bond paper, transparent film	2.5-20	(44~81) $*10^{-3}$	2.0-7.5	50-54	56-59	5.3-5.5	~1.42
Fukai et al. (1995)	Water	Pyrex glass plates and a plate coated with wax	1.5-3.8	3.6	1	72.8	~3000 and ~8000	~60 and ~360	~2 to ~6
Scheller et al. (1995)	Glycerin-water-ethanol mixture	polystyrene and glass	4.9	0.8-4	1-300	65-72	20-$2*10^4$	0.002-0.585 (Oh)	1.5-5.5
Pasandideh-Fard et al. (1996)	Water, 100 and 1000 ppm SDS solution	stainless steel	1	~2.0	1	50, 70, 73	2112	27	2.15-2.62
Mao et al. (1997)	water, aqueous sucrose solution	wax, stainless steel, glass	0.55, 1.86, 2.77, 4,58	2.5, 2.6, 2.7	1.0, 2.0, 16.4	72.8	1485-$1.0*10^4$	11.2-513	1.65-4.94
Thoroddsen et al. (1998)	Fluorescent water solution	glass	N/A	5.5	1	60	~ $1.5*10^4$	~ 1000	4.5-5.2

Table 1: Summary of the parameters from important experiments on droplet impingement on dry surface (From Ok (2005)) (continued)

Authors (Year)	Liquids	Surfaces	V (m/s)	d (mm)	μ (cP)	σ (mN/m)	Re	We	d^*_{max}
Bergeron et al. (2000)	Wate, dilute polyethylene oxide solution	glass coated with a acid complex agent	~3	~2	1	73	6000	250	~4.2
Crooks et al. (2001)	Water, glycerol, PEO solution, surfactant solution	glass, Parafilm M, Perspex, dichloro -silane, and PS	1-3	2.3	1-64	35-73	440-1320	30-300	2-4
Kim et al. (2001)	Deionized water, Ink, Silicone oil	Polycarbo-nate, Silicone oxide	0.77-3.47	2.8-3.7	0.867, 2.6, 36.3	71.7, 55, 37.3	120-$1.4*10^4$	30-582	2.3-3.2
Sikalo et al. (2002)	water, isopropanol, and glycerin	glass, wax, and PVC	1.17-4.55	2.7-3.3	1, 2.4, 116	21, 73, 63	500-$1.5*10^4$	50-1000	2-6
Richard et al. (2002)	Water	Super-hydrophobic surface	0.2-2.3	0.2-8	1	73	N/A	0.3-37	N/A
Rioboo et al. (2002)	Acetone, isopropanol, ethanol, water, silicone oils, glycerine/ water	glasses, PVC, wax, polymer coatings, AKD	0.78-4.1	1.2-4.9	0.3-934	N/A	9-8842	33-396	2.3-5.2
Park et al. (2003)	Water, n-octane, n-tetradecane, n-hexadecane	glass, silicon wafers, Teflon	0.082-4	2.3	1	73	180-5513	0.2-176	2-4
Kim et al. (2003)	Distilled water	Poly-carbonate surface	8-16.2	0.213-0.26	1	73	1700-3900	190-860	3.2-4.4

The effect of polymer additives is studied by several authors [Bergeron et al. (2000); Crook et al. (2001)]. Polymer additives are used to increase the extensional viscosity of the liquid, which is a material property of a fluid to characterize the resistance to stretching. They showed that the height of rebounding is reduced when extensional viscosity is increased.

Effects of surface tension of the liquid droplet were studied [Zhang et al. (1997); Mourougou-Candoni et al. (1999)] mainly by using surfactant in liquids. The use of surfactant is to decrease the surface tension of the fluids. They found that the maximum spread factor increased by adding surfactant into the liquids.

2.2 The Navier-Stokes based computational methods for multiphase flow

There are two main traditional numerical approaches that have been employed to study the multiphase flow problems: front capturing methods and front tracking methods. Here, we will mainly discuss the front capturing methods since they are often employed to study the problems of droplet impingement on surfaces. Front tracking methods will be briefly discussed in section 2.2.2.

2.2.1 Front capturing method

Front capturing methods 'capture' the two-phase interface between a known number of computational cells. In other words, the interface is known to be located somewhere between two locations, but the exact location needs to be constructed numerically. There are several types of front capturing methods: Marker-and-Cell (MAC), Volume-of-Fluid (VOF) and Level-Set method (LSM).

The first numerical simulation of droplet impact was reported by Harlow and Shannon (1967), using so-called "Marker-and-Cell" (MAC) finite difference method, which was proposed by Harlow and Welch in 1965. In the original MAC method, the Navier-Stokes equations were

solved using an Eulerian grid. Lagrangian marker particles are used to identify Fluid 2. For a computational cell without a marker particle, it is considered empty without fluid 2, but filled with fluid 1. For a cell with a marker particle, but lying adjacent to an empty cell, it is called a surface cell. All other cells are considered to be filled with fluid 2. A schematic view of MAC method is shown in Figure 2.

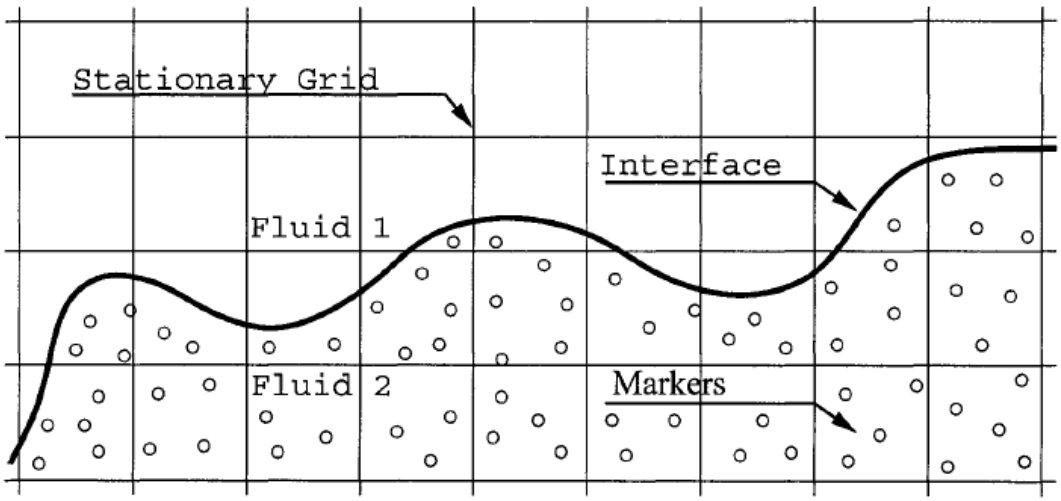

Figure 2: Schematic view of Marker-and-Cell method (From McCracken (2004))

However, in Harlow and Shannon's study, all viscous, surface tension and wetting effects are neglected in their modeling. Thus, their model is only applicable to the initial stages of droplet impact when these effects are negligible due to inertia effect, and their calculations could not predict the maximum spread factor during the impact. In a separate study of high-speed droplets impinging on rigid plane conducted by Huang et al. (1973), they proved MAC method was capable of calculating the peak liquid pressures immediately after the impact, making it useful in research on erosion of turbine blades by high-speed impinging drops.

Later, in the work by Tsurutani et al. (1990), they developed a modified MAC method, called "SMAC-simplified marker and cell", to study the deformation process of a droplet impinging upon a hot flat surface. Surface tension and viscous effects were successfully incorporated in the SMAC method. The numerical calculation was carried out on cylindrical coordinates assuming axisymmetric deformation of the droplet. The dimensionless spreading radius and dimensionless height at any dimensionless time obtained by the numerical calculation showed very good agreement with the experiments conducted by the same group at the same Reynolds number and Weber number. Since convection and evaporation were neglected, the computed temperature profile was only showed qualitatively.

The major shortcoming of MAC method is that a large amount of computational time is consumed to track all the marker particles since a large number is required in order to accurately determine the interface. To overcome this drawback, another numerical method, called Volume of Fluid (VOF) was invented by Hirt and Nichols (1981). The method of VOF is based on the idea of the so-called fraction function C, which is defined as integral function of fluid's characteristic function in every computational cell. Thus, instead of tracking several marker particles in a cell, a single marker function C is used to identify the fluid phase. If the cell is empty (no tracer fluid inside the cell), C=0; if the cell is filled with tracer fluid, then C=1; and when $0<C<1$, that means the interface between two phases cut across the cell. Trapaga and Szekely (1991) employed the "SOLA-VOF" (Solution Algorithm of VOF) to study the influence of surface tension, viscosity and surface wetting properties on the spread factor evolution.

Pasandideh-Fard et al. (1996) developed a modified version of SOLA-VOF method to model the droplet deformation after impact on a solid surface. They used measured values of dynamic contact angles as a boundary condition for the numerical model, and accurate predictions were obtained for droplet diameter during spreading and at equilibrium.

In general, the VOF algorithm consists of two steps: propagation and reconstruction. First, the volume fraction function C at the current time step is solved by the fixed grid, the velocity field and the previous field of C. Second, after the field of C has been updated, the interface will be reconstructed based on the approximation to the section of the interface in each cut cell. The simplest types of VOF methods are the simple line interface calculation (SLIC) of Noh & Woodward (1976) or the SOLA-VOF algorithm of Hirt & Nichols (1981). However, these methods of interface reconstruction are only of the first order accuracy of the characteristic length of the computational cell. In a recent study by Rider & Kothe (1998), a more accurate approach, named piecewise linear interface construction (PLIC) algorithm, was employed. The piecewise linear interface reconstruction insures second order spatial accuracy. A schematic view of SLIC and PLIC is shown in Figure 3. A systematic review of VOF methods can be found in the work done by Scardovelli & Zaleski (1999).

The above-mentioned numerical techniques, such as MAC and VOF, are based on fixed grid. Fixed grid posed problems when the interface between two fluids experiences large deformations. In order to solve this problem, Fukai et al. (1993) proposed a new finite element-based technique to model the droplet spreading process. The inertial, viscous, gravitational, and surface tension

effects were accounted for in this technique. In contrast to other earlier studies of the droplet impingement process, the Lagrangian approach was employed to facilitate the accurate simulation of the motion of the deforming interface. In a later work by Fukai et al. (1995), wetting effects were also incorporated to enhance the capability of their model. They found that the wettability of the substrate upon which the droplet impinges was found to affect significantly all phases of the spreading process, including the formation and development of the ring structure around the splat.

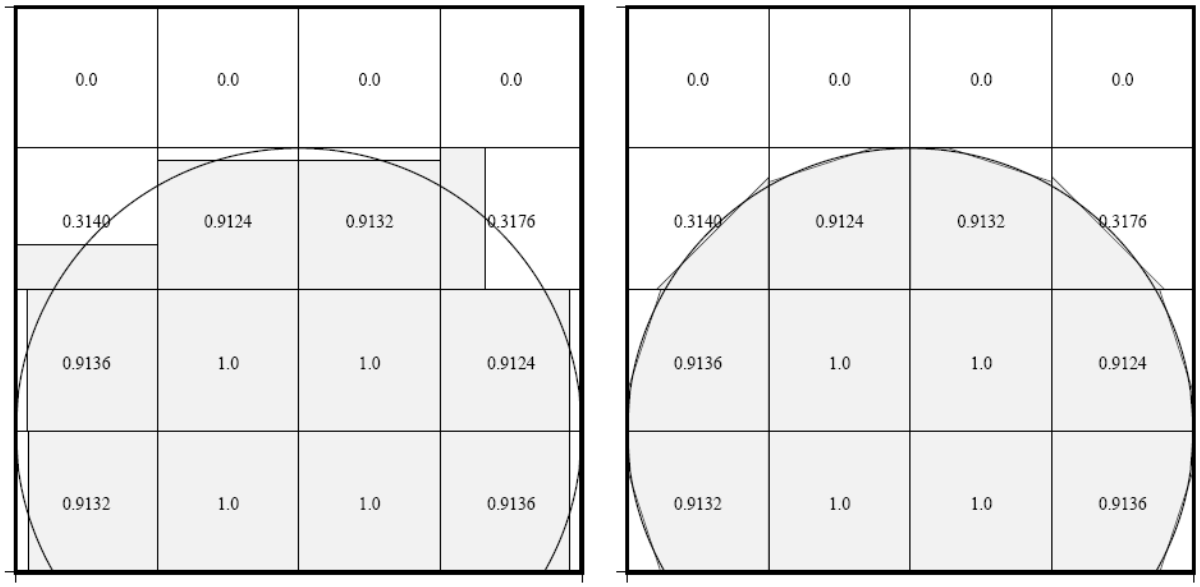

(a) (b)

Figure 3: Two ways to reconstruct the interfaces (shaded areas) for a circle (continuous line) (a) First-order or simple line interface calculation (SLIC); (b) second-order or piecewise linear interface construction (PLIC) (From Rider & Kothe (1998))

Very similar to VOF method, Osher & Sethian (1988) proposed a level-set method (LSM) for capturing the interfaces. In LSM, a level-set parameter, φ is used to define two phases. When

$\varphi > 0$, it is considered as phase 1; when $\varphi < 0$, it is considered phase 2; $\varphi = 0$ is considered where the interface between two phases exits. The computations are carried out on fixed grids. However, unlike VOF, the LSM does not involve interface reconstruction. A recent review is done by Sethian & Smereka (2003). This method has not been used in the study of droplet impingement on surfaces.

2.2.2 Front tracking method

Unlike front capturing methods, front tracking methods directly 'track' the location of the interface between different phases instead of constructing the interface. As reviewed by McCracken (2004), the major types of front tracking methods are: boundary-fitted grid method, fixed grid method, hybrid method, and Boundary Element Method (BEM).

Haller et al. (2002) investigated the fluid dynamics of high-speed (500 m/s) small size (0.2 mm in diameter) droplet impact on a rigid substrate using a front tracking solution procedure, named FronTier, which was originally proposed by Glimm et al. (1998). They found that compressible flow patterns dominate the early droplet impact process and splashing. Their simulations showed that upon collision, a shock wave attached to the contact edge of the droplet was generated. The liquid zone adjacent to the target surface was highly compressed and bounded by the shock envelope, which separated it from the unaffected bulk of the liquid. Subsequently, the radial velocity of the contact edge decreased below the shock velocity. The pressure difference across the free surface at the contact edge region triggered the eruption of intense lateral jetting of high velocity.

2.3 Theoretical approach for multiphase flows

Several theoretical modeling for predicting the maximum spreading factor during the impingement process are reviewed in this section, and the relevant correlations are listed in Table 2. Most of models are based on an energy balance with some assumptions made on the dissipated energy term. Two states are usually chosen: the state just before the drop hits the surface and the state when the drop reaches maximum spreading factor on the surface. The energy balance can be written by:

$$E_k + E_p + E_s = E_k^{'} + E_p^{'} + E_s^{'} + E_d^{'} \tag{2.1}$$

where E_k, E_p, E_s and E_d are the kinetic, potential, surface, dissipated energies respectively. The corresponding primed quantities are after impact.

Table 2: Summary of theoretical models to predict maximum spread factor (From Ok (2005))

Authors	Models
Chandra et al. (1991)	$\frac{3}{2}\frac{We}{\mathrm{Re}}(d_{\max}^*)^4 + (1-\cos\theta)(d_{\max}^*)^2 - (\frac{1}{3}We + 4) = 0$
Asai et al. (1993)	$d_{\max}^* = 1 + 0.48We^{0.5}\exp(-1.48We^{0.22}\,\mathrm{Re}^{-0.21})$
Scheller et al. (1995)	$d_{\max}^* = 0.61(\mathrm{Re}^2\,Oh)^{0.166}$
Fukai et al. (1995)	$\frac{1}{2}\frac{We}{\mathrm{Re}^{0.772}}(d_{\max}^*)^4 + 2.29(1-\cos\psi)(d_{\max}^*)^2 - (\frac{1}{3}We + 4) = 0$
Pasandideh-Fard et al. (1995)	$d_{\max}^* = \sqrt{\frac{We+12}{3(1-\cos\theta_a) + 4(We/\sqrt{\mathrm{Re}})}}$ For $We \gg \sqrt{\mathrm{Re}}$, $d_{\max}^* \approx 0.5\,\mathrm{Re}^{0.25}$
Mao et al. (1997)	$\left[\frac{1}{4}(1-\cos\theta) + 0.2(\frac{We^{0.83}}{\mathrm{Re}^{0.33}})\right](d_{\max}^*)^3 - (\frac{We}{12}+1)d_{\max}^* + \frac{2}{3} = 0$
Notation: θ: equilibrium contact angle ψ: dynamic contact angle θ_a: advancing contact angle	

Although there are various correlations derived from experiments or theoretical calculations, Rioboo et al. (2001) claimed that the thresholds between various outcomes in Figure 1 can not be simply quantified in terms of the dimensionless groups, We, Re, Oh and K ($K=We*Oh^{-0.4}$), a clear manifestation that these dimensionless groups are insensitive to the surface wettability and roughness effects, which are of the utmost importance in the drop impingement on a dry surface.

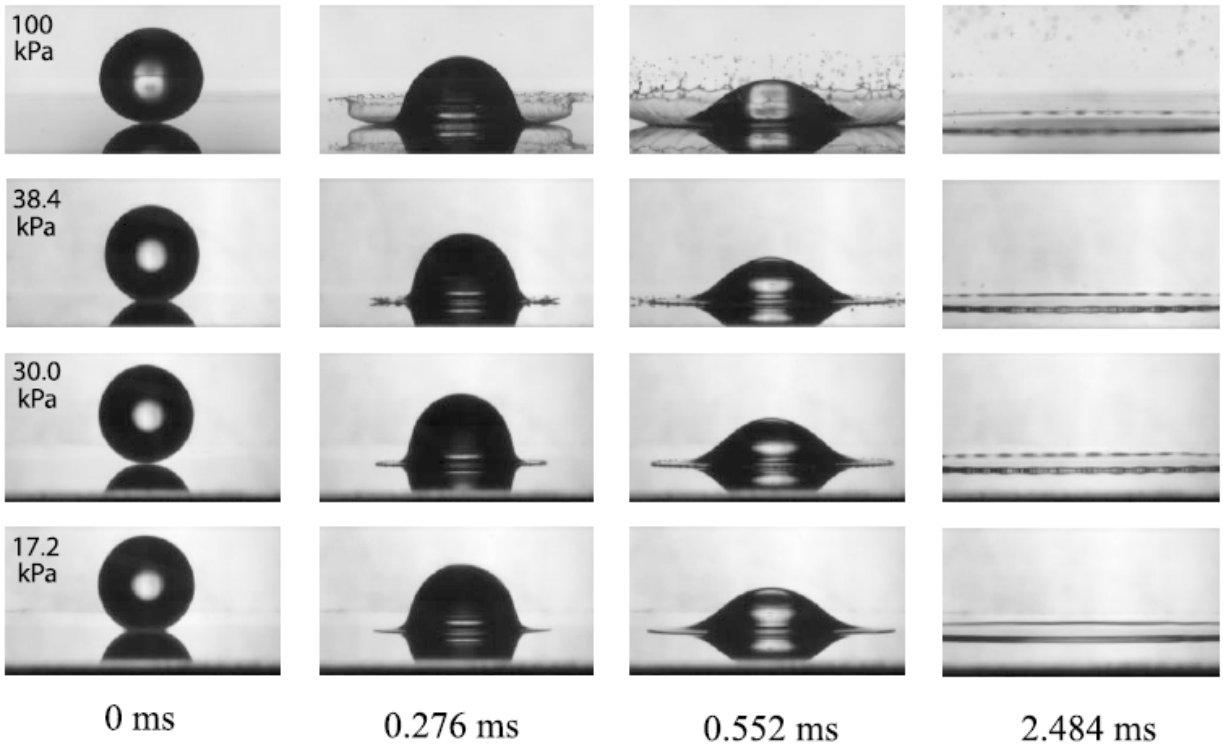

Figure 4: Photographs of a liquid drop hitting on a smooth dry substrate at different surrounding pressure (From Xu et al. (2005))

For all the previous studies, including experimental and numerical work, the surrounding medium of the gas phase was not considered to have any influence on the impingement outcome. However, in a very recent study by Xu et al. (2005), they found that the pressure or the

molecular weight of surrounding gas phase is critical for the impingement outcome of splashing or not. By decreasing the surrounding pressure or using gas with low molecular weight, the splashing can be completely depressed. The results of their experiments are shown on Figure 4.

2.4 Lattice Boltzmann schemes for multiphase flows

The lattice Boltzmann method (LBM) is a relatively new technique for simulating fluid flows and modeling physics in fluids. So far, it has shown great success in fluid flow applications involving interfacial dynamics and complex geometries (Chen & Doolen (1998)), and it is still under development. So far, there have been a number of multiphase flow LBM models existing in literature.

Gunstensen et al. (1991) first developed the multiphase LBM method using two particle distribution functions. This method introduced unphysical velocity currents at the interface. In addition, this method would not be applicable to our current problem where densities of the two phases need to be different.

In the first methodology that used different densities for phases, Shan & Chen (1993) proposed what is so-called pseudo-potential LBM model using non-local interaction between particles. Despite the high spurious currents at the interface, several researchers have used this method [Yuan & Laura (2006); Shan & Doolen (1995); Sankaranarayanan et al. (1999, 2002)]. Later, Swift et al. (1995, 1996) proposed a famous thermodynamic based LBM model, which is also

known as free energy approach. More details for the review of all those multiphase LBM models will be provided in Section 4.1.

All LBM schemes mentioned above are restricted to small density ratios which are less than 10, and suffer from instability when dealing with larger density ratios. By modifying the free energy approach, Inamuro et al. (2004) first proposed an LBM scheme which is able to deal with such two-phase fluid flows of density ratio up to 1000. More recently, Lee and Lin (2005) devised a new LBM scheme which enables stable simulation of two-phase flows with high density and viscosity ratios. However, they reported that their method introduces anisotropy due to the special treatment of discretization of the forcing terms in the lattice Boltzmann equation.

So far, there have been a few studies dealing with liquid-wall interaction using LBM (Briant et al. (2004); Mo et al. (2005); Kang et al. (2005)). These studies have separately validated their method by using Young's equation, according to which the static contact angle between the liquid-gas interface and the wall is an outcome of the surface tension forces between the three phases: liquid, gas and solid. However, there are only two prior studies of droplet impact on a dry surface using LBM. The first one, by Mukherjee and Abraham (2007), employed an axi-symmetric LBM model to study the impact of a droplet on a wall within a density ratio of 10. They found that a droplet impinging on a super hydrophobic surface may completely lift off from the surface, leading to a rebound. In another separate work, Gupta and Kumar (2008) systematically studied the droplet spreading diameter at various Weber and Reynolds number by using the pseudo-potential model, and found that droplet impinging on a non-wetting surface

may result in an in-plane break-up of the spreading film. Again, their simulations were done within a density ratio of 10. In this present study, a relatively high density ratio of 50 will be used for entire simulations.

CHAPTER THREE: LATTICE BOLTZMANN METHOD

3.1 History review of LBM from LGA

LBM originated from lattice gas automation (LGA) method, a discrete particle kinetic method involving discrete lattice and discrete time. In LGA, the motion of gas or liquid particles is constrained only through the lattice. The first LGA model with full discretized particle velocity, space and time was proposed by Hardy, de Pazzis and Pomeau (1976), also known as HPP model. In HPP model, the lattice is square, and the particles can only move axially, but not diagonally. Thus, the HPP model is highly anisotropic. Later, in 1986, Frisch, Hasslacher and Pomeau (1986) introduced a LGA model employing a hexagonal lattice, as shown in Figure 5. They recognized that lattice symmetry is very important to recover the Navier-Stokes equations. Also because of higher symmetry, the hexagonal lattice does not suffer as large anisotropy troubles as of HPP's square lattice.

In LGA, a set of Boolean variables $n_i(\mathbf{x},t)(i=0,1,2....,M)$ describing the particle occupation number at space and time $(\mathbf{x},t)$ is defined. The concept of occupation number n_i is borrowed from statistical mechanics. The evolution equation of LGA is given as:

$$n_i(\mathbf{x}+\mathbf{e}_i,t+1)=n_i(\mathbf{x},t)+\Omega_i(n(\mathbf{x},t)) \tag{3.1}$$

Where $\mathbf{e}_i$ is discretized particle velocity in direction i, and $\Omega_i(n(\mathbf{x},t))$ is the collision operator. This evolution equation consists of two sub-steps at every time step:

Collision: $n_i^p(\mathbf{x},t) - n_i(\mathbf{x},t) = \Omega_i(n(\mathbf{x},t))$ (3.2a)

Streaming: $n_i(\mathbf{x}+\mathbf{e}_i, t+1) = n_i^p(\mathbf{x},t)$ (3.2b)

Where n_i^p means post-collision quantity of particle occupation number.

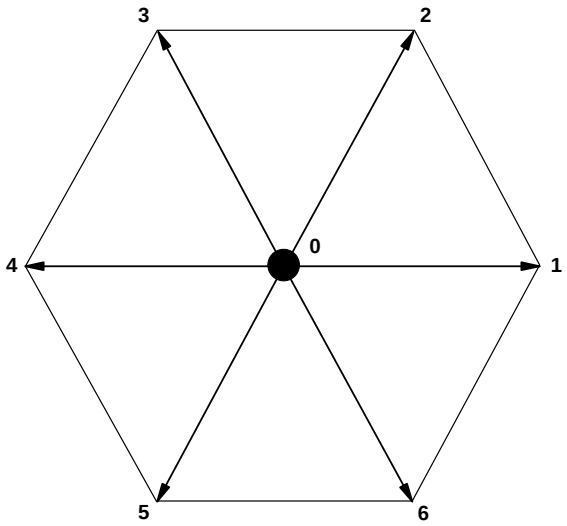

Figure 5: D2Q7 lattice structure

However, the major drawback of LGA is that it suffers large statistical noise. Under this background, McNamaro & Zanetti (1988) invented the earliest LBM scheme, in which the particle occupation number n_i is replaced by single particle distribution function, f_i. This is the first time that the lattice Boltzmann equation was used in numerical calculations and it brought a whole new perspective in the area of computational fluid dynamics (CFD). In LBM, instead of tracking single Boolean particle, we follow the averaged particle distribution function, which means the probability of finding a particle at a given location and a given time. This procedure

eliminates statistical noise in the LBM. And because of the averaged kinetic equations and variables, LBM is a kind of mesoscopic method.

In the above sense, LBM may be essentially considered as an improvement of the LGA. On the other hand, it was also believed that the LBE could be directly connected to the Boltzmann equation, which is a well known kinetic equation in non-equilibrium statistical mechanics, describing the evolution of particle populations in terms of distribution functions. Later, He & Luo (1997) successfully derived LBE starting from the continuum Boltzmann equation. We will show the details in next section.

3.2 From Boltzmann equation to lattice Boltzmann equation

We start this section by the well known Boltzmann equation, i.e.:

$$\frac{Df}{Dt} = \frac{\partial f}{\partial t} + \boldsymbol{\xi} \bullet \nabla f + \mathbf{F} \bullet \nabla_{\xi} f = \left. \frac{\partial f}{\partial t} \right|_{collision} \tag{3.3}$$

where $f \equiv f(\mathbf{x}, \boldsymbol{\xi}, t)$ represents the single-particle distribution function in the phase space $(\mathbf{x}, \boldsymbol{\xi})$, x is the position in space, $\boldsymbol{\xi}$ is the microscopic velocity, F is the external force. The term on the right hand side of the equation is the collision term, which accounts for the change of particle distribution function due to the collision. Here, we are using the Bhatnagar-Gross-Krook (BGK) collision operator. Hence,

$$\left. \frac{\partial f}{\partial t} \right|_{collision} = -\frac{1}{\lambda}(f - f^{eq}) \tag{3.4}$$

where λ is the relaxation time due to collision, and f^{eq} is the Boltzmann-Maxwellian distribution, given by:

$$f^{eq} = \frac{\rho}{(2\pi RT)^{D/2}} \exp\left[-\frac{(\xi - \mathbf{u})^2}{2RT} \right] \tag{3.5}$$

where R is the ideal gas constant, D is the dimension of space, ρ, $\mathbf{u}$ and T are fluid density, velocity and temperature, respectively. The macroscopic variables, ρ, $\mathbf{u}$ and T can be computed from the moments of the distribution function, given as

$$\rho = \int f d\xi = \int f^{eq} d\xi \tag{3.6a}$$

$$\rho \mathbf{u} = \int \xi f d\xi = \int \xi f^{eq} d\xi \tag{3.6b}$$

$$\rho \varepsilon = \frac{1}{2} \int (\xi - \mathbf{u})^2 \, f d\xi = \frac{1}{2} \int (\xi - \mathbf{u})^2 \, f^{eq} d\xi \tag{3.6c}$$

where ε is the internal energy, which can be written in terms of temperature:

$$\varepsilon = \frac{D}{2} RT = \frac{D}{2} N_A k_B T \tag{3.7}$$

where N_A is Avogadro's number and k_B is the Boltzmann constant. Thus,

$$\rho DRT = \int (\xi - \mathbf{u})^2 \, f d\xi = \int (\xi - \mathbf{u})^2 \, f^{eq} d\xi \tag{3.8}$$

Here we only consider the system without external force, $\mathbf{F} \equiv 0$. Therefore, the Boltzmann equation becomes:

$$\frac{\partial f}{\partial t} + \xi \bullet \nabla f = -\frac{1}{\lambda} (f - f^{eq}) \tag{3.9}$$

Use the total derivative notation, $\frac{d}{dt} = \frac{\partial}{\partial t} + \xi \bullet \nabla$, we can simplify the Boltzmann equation to:

$$\frac{df}{dt}+\frac{1}{\lambda}f=\frac{1}{\lambda}f^{eq} \tag{3.10}$$

The equation above is written in form of an ordinary differential equation. Integrate the above equation over a time step δ_t, we can get:

$$f(\mathbf{x}+\xi\delta_t,\xi,t+\delta_t)=\frac{1}{\lambda}e^{-\delta_t/\lambda}\int_0^{\delta_t}e^{t'/\lambda}f^{eq}(\mathbf{x}+\xi t',\xi,t+t')dt'+e^{-\delta_t/\lambda}f(\mathbf{x},\xi,t) \tag{3.11}$$

Assuming that δ_t and f^{eq} is smooth enough locally, by using linear interpolation, the equilibrium distribution function can be approximated as follows:

$$f^{eq}(\mathbf{x}+\xi t',\xi,t+t')=f^{eq}(\mathbf{x},\xi,t)+\frac{t'}{\delta_t}\left[f^{eq}(\mathbf{x}+\xi\delta_t,\xi,t+\delta_t)-f^{eq}(\mathbf{x},\xi,t)\right]+O(\delta_t^2) \tag{3.12}$$

With $0\le t'\le\delta_t$. Simplify the equation,

$$f^{eq}(\mathbf{x}+\xi t',\xi,t+t')=(1-\frac{t'}{\delta_t})f^{eq}(\mathbf{x},\xi,t)+\frac{t'}{\delta_t}f^{eq}(\mathbf{x}+\xi\delta_t,\xi,t+\delta_t)+O(\delta_t^2) \tag{3.12}$$

The above order of accuracy are of the order of $O(\delta_t^2)$. Substituting the above equation into Eq. (3.11), we can get:

$$\begin{aligned}f(\mathbf{x}+\xi\delta_t,\xi,t+\delta_t)-f(\mathbf{x},\xi,t)&=(e^{-\delta_t/\lambda}-1)\left[f(\mathbf{x},\xi,t)-f^{eq}(\mathbf{x},\xi,t)\right]\\&+\left[1+\frac{\lambda}{\delta_t}(e^{-\delta_t/\lambda}-1)\right]\left[f^{eq}(\mathbf{x}+\xi\delta_t,\xi,t+\delta_t)-f^{eq}(\mathbf{x},\xi,t)\right]\end{aligned} \tag{3.13}$$

Performing Taylor expansion for the term $e^{-\delta_t/\lambda}$, as of the order of $O(\delta_t^2)$, we get:

$$e^{-\delta_t/\lambda}=1-\delta_t/\lambda+O(\delta_t^2) \tag{3.14}$$

Substitute it into Eq. (3.13), and simplify the equation, we can get:

$$f(\mathbf{x}+\xi\delta_t,\xi,t+\delta_t)-f(\mathbf{x},\xi,t)=-\frac{1}{\tau}\left[f(\mathbf{x},\xi,t)-f^{eq}(\mathbf{x},\xi,t)\right] \tag{3.15}$$

where $\tau \equiv \lambda / \delta_t$ is the dimensionless relaxation time with the scaling time of δ_t. Hence, Eq. (15) is accurate to the first order in δ_t, and it is the time evolution equation of the distribution function f. Although $f^{eq}(\mathbf{x},\boldsymbol{\xi},t)$ is written as an explicit function of time t, its time dependence is in the hydrodynamic variables, ρ, $\mathbf{u}$ and T. Thus, we can interpret the equilibrium distribution function as of $f^{eq}(\mathbf{x},\boldsymbol{\xi};\rho,\mathbf{u},T)$. Thus, it is important to calculate ρ, $\mathbf{u}$ and T in discretizing the Boltzmann equation.

In order to numerically evaluate the hydrodynamic moments, appropriate discretization in velocity space $\boldsymbol{\xi}$ must be accomplished. Employing

$$\int \psi(\boldsymbol{\xi}) f^{eq}(\mathbf{x},\boldsymbol{\xi},t) d\boldsymbol{\xi} = \sum_{\alpha} W_\alpha \psi(\boldsymbol{\xi}_\alpha) f^{eq}(\mathbf{x},\boldsymbol{\xi}_\alpha,t) \tag{3.16}$$

where $\psi(\boldsymbol{\xi})$ is a polynomial of $\boldsymbol{\xi}$, W_α is the weight coefficient of the quadrature and $\boldsymbol{\xi}_\alpha$ is the discrete velocity set or the abscissas of the quadrature. Accordingly, the hydrodynamic moments of Eqs. (3.6a)-(3.6c) can be evaluated as:

$$\rho = \sum_{\alpha} f_\alpha = \sum_{\alpha} f_\alpha^{eq} \tag{3.17a}$$

$$\rho \mathbf{u} = \sum_{\alpha} \boldsymbol{\xi}_\alpha f_\alpha = \sum_{\alpha} \boldsymbol{\xi}_\alpha f_\alpha^{eq} \tag{3.17b}$$

$$\rho \varepsilon = \frac{1}{2} \sum_{\alpha} (\boldsymbol{\xi} - \mathbf{u})^2 f_\alpha = \frac{1}{2} \sum_{\alpha} (\boldsymbol{\xi} - \mathbf{u})^2 f_\alpha^{eq} \tag{3.17c}$$

where

$$f_\alpha \equiv f_\alpha(\mathbf{x},\boldsymbol{\xi},t) \equiv W_\alpha f(\mathbf{x},\boldsymbol{\xi}_\alpha,t) \tag{3.18a}$$

$$f_\alpha^{eq} \equiv f_\alpha^{eq}(\mathbf{x},\boldsymbol{\xi},t) \equiv W_\alpha f^{eq}(\mathbf{x},\boldsymbol{\xi}_\alpha,t) \tag{3.18b}$$

The equilibrium distribution function is obtained from a truncated small velocity expansion or low-Mach number approximation:

$$f^{eq} = \frac{\rho}{(2\pi RT)^{D/2}} \exp\left[-\frac{(\boldsymbol{\xi} - \mathbf{u})^2}{2RT} \right]$$

$$= \frac{\rho}{(2\pi RT)^{D/2}} \exp(-\frac{\xi^2}{2RT}) \exp(\frac{\boldsymbol{\xi} \bullet \mathbf{u}}{RT} - \frac{\mathbf{u}^2}{2RT})$$

$$= \frac{\rho}{(2\pi RT)^{D/2}} \exp(-\frac{\xi^2}{2RT}) \times \left[1 + \frac{\boldsymbol{\xi} \bullet \mathbf{u}}{RT} + \frac{(\boldsymbol{\xi} \bullet \mathbf{u})^2}{2(RT)^2} - \frac{\mathbf{u}^2}{2RT} \right] + O(\mathbf{u}^3)$$

$$f^{eq} = \frac{\rho}{(2\pi RT)^{D/2}} \exp(-\frac{\xi^2}{2RT}) \times \left[1 + \frac{\boldsymbol{\xi} \bullet \mathbf{u}}{RT} + \frac{(\boldsymbol{\xi} \bullet \mathbf{u})^2}{2(RT)^2} - \frac{\mathbf{u}^2}{2RT} \right] \tag{3.19}$$

Although above equation for f^{eq} only retains the terms up to $O(\mathbf{u}^2)$, it could also be expanded to higher-order in terms of $\mathbf{u}$, if necessary.

Now, two factors have been taken into consideration in the discretization of phase space. First, the discretized velocity space is coupled to the configuration space such that a specific lattice structure is obtained. Second, quadrature must be accurate enough such that not only the conservation constraints are preserved, but also the symmetry requirement in the Navier-Stokes equations is satisfied, i.e., isotropy of the stress tensor. In the next section of this chapter, it will be shown that Navier-Stokes equation can be derived from LBE via the Chapman-Enskog analysis. In order for this to happen, the quadrature used to compute the hydrodynamic moments must be able to compute the following moments with respect to f^{eq} exactly:

$$\rho : 1, \xi_i, \xi_i \xi_j \tag{3.20a}$$

$$\mathbf{u}: \xi_i, \xi_i\xi_j, \xi_i\xi_j\xi_k \tag{3.20b}$$

where ξ_i is the component of $\boldsymbol{\xi}$ in Cartesian coordinates. Computing the hydrodynamic moments of f^{eq} is equivalent to evaluating the following integral

$$I = \int \psi(\boldsymbol{\xi}) f^{eq} d\boldsymbol{\xi} = \frac{\rho}{(2\pi RT)^{D/2}} \int \psi(\boldsymbol{\xi}) \exp(-\frac{\boldsymbol{\xi}^2}{2RT}) \times \left[1 + \frac{\boldsymbol{\xi} \bullet \mathbf{u}}{RT} + \frac{(\boldsymbol{\xi} \bullet \mathbf{u})^2}{2(RT)^2} - \frac{\mathbf{u}^2}{2RT} \right] d\boldsymbol{\xi} \tag{3.21}$$

where $\psi(\boldsymbol{\xi})$ is a polynomial of $\boldsymbol{\xi}$. The above integral is of the following type: $\int e^{-x^2} \psi(x) dx$, which can be evaluated numerically with a Gauss-type quadrature. Our objective is to evaluate the hydrodynamic moments. Here, the two-dimensional, nine-velocity (D2Q9) model invented by Qian et al. (1992) is employed. The lattice structure is shown in Figure 6. To recover this set of discrete set of velocities, $\psi(\boldsymbol{\xi})$ is set to:

$$\psi_{m,n}(\boldsymbol{\xi}) = \xi_x^m \xi_y^n \tag{3.22}$$

where ξ_x and ξ_y is x and y component of $\boldsymbol{\xi}$. Now, the integral of moments in Eq. (3.21) becomes:

$$\begin{aligned} I = \int \psi_{m,n}(\boldsymbol{\xi}) f^{eq} d\boldsymbol{\xi} = \frac{\rho}{\pi} (\sqrt{2RT})^{m+n} \Bigg\{ & (1 - \frac{\mathbf{u}^2}{2RT}) I_m I_n + \\ & \frac{2(u_x I_{m+1} I_n + u_y I_m I_{n+1})}{\sqrt{2RT}} + \frac{u_x^2 I_{m+2} I_n + 2u_x u_y I_{m+1} I_{n+1} + u_y^2 I_m I_{n+2}}{RT} \Bigg\} \end{aligned} \tag{3.23}$$

where

$$I_m = \int_{-\infty}^{+\infty} e^{-\zeta^2} \zeta^m d\zeta, \qquad \zeta = \xi / \sqrt{2RT} \tag{3.24}$$

is the m th order moment of the weight function, $e^{-\zeta^2}$ on the real axis. Employing a third-order Hermite formula, I_m may be expressed as:

$$I_m = \sum_{j=1}^{3} \omega_j \zeta_j^m \tag{3.25}$$

The three abscissas of the quadrature are:

$$\zeta_1 = -\sqrt{3/2},\ \zeta_2 = 0,\ \zeta_3 = \sqrt{3/2} \tag{3.26}$$

and the corresponding weight coefficients are:

$$\omega_1 = \sqrt{\pi}/6,\ \omega_2 = 2\sqrt{\pi}/3,\ \omega_3 = \sqrt{\pi}/6 \tag{3.27}$$

Then the integral of the moment in Eq. (3.23) becomes

$$I = \frac{\rho}{\pi} \sum_{i,j=1}^{3} \omega_i \omega_j \psi(\boldsymbol{\xi}_{i,j}) \left\{ 1 + \frac{\boldsymbol{\xi}_{i,j} \bullet \mathbf{u}}{RT} + \frac{(\boldsymbol{\xi}_{i,j} \bullet \mathbf{u})^2}{2(RT)^2} - \frac{\mathbf{u}^2}{2RT} \right\} \tag{3.28}$$

where $\boldsymbol{\xi}_{i,j} = (\xi_i, \xi_j) = \sqrt{2RT}\,(\zeta_i, \zeta_j)$. Comparing Eq. (3.21) and Eq. (3.28), we can identify:

$$f_{i,j}^{eq} = \frac{\omega_i \omega_j}{\pi} \rho \left\{ 1 + \frac{\boldsymbol{\xi}_{i,j} \bullet \mathbf{u}}{RT} + \frac{(\boldsymbol{\xi}_{i,j} \bullet \mathbf{u})^2}{2(RT)^2} - \frac{\mathbf{u}^2}{2RT} \right\} \tag{3.29}$$

With the discrete velocities defined as:

$$e_\alpha = \begin{cases} (0,0) & \alpha = 0 \\ (\cos\theta_\alpha, \sin\theta_\alpha)c & \theta_\alpha = (\alpha - 1)\pi/2 \quad \alpha = 1,2,3,4 \\ \sqrt{2}(\cos\theta_\alpha, \sin\theta_\alpha)c & \theta_\alpha = (\alpha - 5)\pi/2 + \pi/4 \quad \alpha = 5,6,7,8 \end{cases} \tag{3.30}$$

where $c = \dfrac{\delta_x}{\delta_t}$, δ_x is the lattice spacing, δ_t is the advection time for the particle to travel from one site to the adjacent site along coordinate directions.

$$w_\alpha = \frac{\omega_i \omega_j}{\pi} = \begin{cases} 4/9 & i = j = 2 \quad \alpha = 0 \\ 1/9 & i = 1, j = 2, ... \quad \alpha = 1,2,3,4 \\ 1/36 & i = j = 1, ... \quad \alpha = 5,6,7,8 \end{cases} \tag{3.31}$$

Now substituting $RT = c_s^2 = c^2/3$, the final form of equilibrium distribution function for D2Q9 lattice structure is obtained:

$$f_\alpha^{eq} = w_\alpha \rho \left\{ 1 + \frac{3(e_\alpha \bullet \mathbf{u})}{c^2} + \frac{9(e_\alpha \bullet \mathbf{u})^2}{2c^4} - \frac{3\mathbf{u}^2}{2c^2} \right\} \tag{3.32}$$

Finally, the time-discrete version of Boltzmann equation is given by:

$$f_\alpha(\mathbf{x} + \xi\delta_t, \xi, t + \delta_t) - f_\alpha(\mathbf{x}, \xi, t) = -\frac{1}{\tau}\left[f_\alpha(\mathbf{x}, \xi, t) - f_\alpha^{eq}(\mathbf{x}, \xi, t) \right] \tag{3.33}$$

In this section, we have systematically shown that the lattice Boltzmann equation can be derived from Boltzmann equation. In the next section, we will show how the Navier-Stokes equations can be derived from the lattice Boltzmann equation.

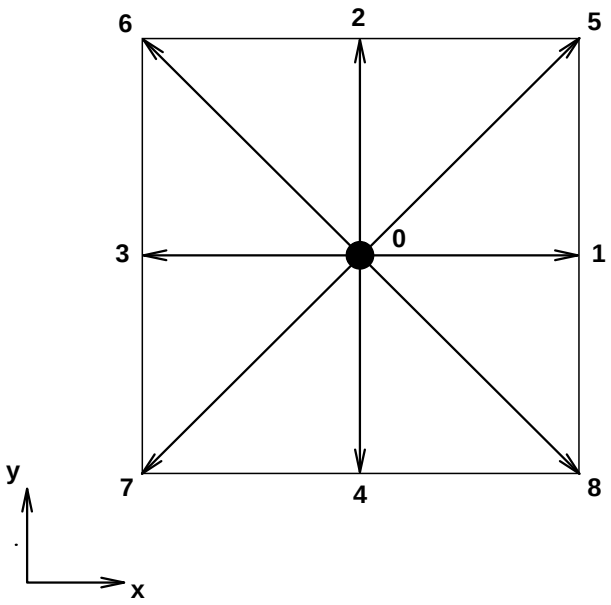

Figure 6: D2Q9 lattice structure

3.3 Derivation of Navier-Stokes equations from LBE

Since the fundamental idea of LBM is to construct simplified kinetic models that incorporate the essential physics of microscopic or mesoscopic processes so that the macroscopic averaged properties obey the desired macroscopic equations (Chen & Doolen (1998)), it is important to derive the Navier-Stokes equations directly from the LBE. In this section, by employing the Chapman-Enskog multiscale expansion technique which is used to solve Boltzmann equation in kinetic theory, the Navier-Stokes equations are successfully derived from LBE. This method has been applied by several authors in the LBM context (Hou et al. (1995); Chen & Doolen (1998)). In this method, an asymptotic expansion is performed with the Knudsen number which acts as small variable of expansion. The requirement of isotropy, Galilean-invariance and velocity independence is imposed during the analysis.

We begin our derivation process by considering the basic BGK model of LBE using the D2Q9 lattice structure. However, the process would be similar for other lattice models.

Tensor properties are very important during the analysis. Following Wolf-Gladrow (2000), the second and fourth order tensors are given as:

$$\sum_i e_{\sigma i\alpha} e_{\sigma i\beta} = 2c^2 e_\sigma^2 \delta_{\alpha\beta} \tag{3.34}$$

where $e_1 = c$, $e_2 = \sqrt{2}c$, and $\delta_{\alpha\beta}$ is the Kronecker delta, i.e.,

$$\delta_{\alpha\beta} = \begin{cases} 1 \ if \ \alpha = \beta \\ 0 \ if \ \alpha \neq \beta \end{cases} \tag{3.35}$$

Similarly,

$$\sum_i e_{\sigma i\alpha} e_{\sigma i\beta} e_{\sigma i\gamma} e_{\sigma i\theta} = \begin{cases} 2c^4 \delta_{\alpha\beta\gamma\theta}, & \sigma = 1 \\ 4c^4 \Delta_{\alpha\beta\gamma\theta} - 8c^4 \delta_{\alpha\beta\gamma\theta}, & \sigma = 2 \end{cases} \tag{3.36}$$

where $\delta_{\alpha\beta\gamma\theta}$ is similarly as $\delta_{\alpha\beta}$, and $\Delta_{\alpha\beta\gamma\theta} = \delta_{\alpha\beta}\delta_{\gamma\theta} + \delta_{\alpha\gamma}\delta_{\beta\theta} + \delta_{\alpha\theta}\delta_{\beta\gamma}$. These lattice tensors upto fourth order are isotropic, and there isotropic nature is important to correctly recover the viscous stress for the fluid.

The general form of LBE with BGK collision operator is given as:

$$f_{\sigma i}(\mathbf{x} + e_{\sigma i}\delta_t, t + \delta_t) - f_{\sigma i}(\mathbf{x}, t) = -\frac{1}{\tau}\left[f_{\sigma i}(\mathbf{x}, t) - f^0_{\sigma i}(\mathbf{x}, t) \right] \tag{3.37}$$

The macroscopic fluid density and velocity are defined as kinetic moments of the distribution functions:

$$\rho = \sum_\sigma \sum_i f_{\sigma i}(\mathbf{x}, t) \tag{3.38a}$$

$$\rho \mathbf{u} = \sum_\sigma \sum_i f_{\sigma i}(\mathbf{x}, t) \tag{3.38b}$$

For ease of presentation of the asymptotic analysis, we let:

$$f^{eq}_{\sigma i}(\mathbf{x}, t) = f^0_{\sigma i}(\mathbf{x}, t) \tag{3.39}$$

Then let the unknown equilibrium distribution function be expanded upto the quadratic term in fluid velocities:

$$f^0_{\sigma i}(\mathbf{x}, t) = A_\sigma + B_\sigma (e_{\sigma i} \bullet \mathbf{u}) + C_\sigma (e_{\sigma i} \bullet \mathbf{u})^2 + D_\sigma \mathbf{u}^2 \tag{3.40}$$

Employing the conservation equations:

$$\sum_\sigma \sum_i f_{\sigma i}(\mathbf{x}, t) = \sum_\sigma \sum_i f^0_{\sigma i}(\mathbf{x}, t) = \rho \tag{3.41a}$$

$$\sum_{\sigma}\sum_{i} f_{\sigma i}(\mathbf{x},t) = \sum_{\sigma}\sum_{i} f^{0}_{\sigma i}(\mathbf{x},t) = \rho\mathbf{u} \tag{3.41b}$$

We will obtain the coefficients below:

$$A_0 + 4A_1 + 4A_2 = \rho \tag{3.42a}$$

$$2C_1 + 4C_2 + D_0 + 4D_1 + 4D_2 = 0 \tag{3.42b}$$

$$2B_1 + 4B_2 = \rho \tag{3.42c}$$

As we mentioned earlier, to facilitate the asymptotic expansion, we will introduce a small parameter, Knudsen number which is the ratio of the mean free path of the molecules to the length scale of the problem. Here, we let the particle advection time to be that small parameter (Hou et al. (1995)), i.e., $\varepsilon = \delta_t$.

Expanding the particle distribution function about its local equilibrium distribution in terms of ε :

$$f_{\sigma i} = f^{0}_{\sigma i} + \varepsilon f^{1}_{\sigma i} + \varepsilon^2 f^{2}_{\sigma i} + O(\varepsilon^3) \tag{3.43}$$

To compute variations of $f_{\sigma i}$ at different time scales, two time scales are introduced following the multi-scale procedure, i.e.,

$t_0 = t$ and $t_1 = \varepsilon t$.

Thus, the procedure for multiple time scales can be written as: $t=t(t_1,t_2)$, following this:

$$\frac{\partial}{\partial t} = \frac{\partial}{\partial t_0} + \varepsilon \frac{\partial}{\partial t_1} + ... \tag{3.44}$$

Substituting Eqs. (3.43) and (3.44) into Eq. (3.37), the $O(\varepsilon)$ equation is:

$$(\partial_{t_0} + e_{\sigma i} \bullet \nabla) f^{0}_{\sigma i} = -\frac{1}{\tau} f^{1}_{\sigma i} \tag{3.45}$$

Similarly, $O(\varepsilon^2)$ is:

$$\partial_{t_1} f_{\sigma i}^0 + (\partial_{t_0} + e_{\sigma i} \bullet \nabla)(1 - \frac{1}{2\tau}) f_{\sigma i}^1 = -\frac{1}{\tau} f_{\sigma i}^2 \tag{3.46}$$

Taking the zeroth kinetic moment of Eq. (3.45) and enforcing the consistency condition, we get:

$$\partial_{t_0} \rho + \nabla \bullet (\rho \mathbf{u}) = 0 \tag{3.47}$$

This is the first order continuity equation. Next, take the first kinetic moment of Eq. (3.45), we get the first order momentum equation:

$$\partial_{t_0} (\rho \mathbf{u}) + \nabla \bullet \Pi^0 = 0 \tag{3.48}$$

where Π^0 is the first-order momentum flux tensor, and it is given by:

$$\Pi^0 = \sum_{\sigma} \sum_{i} e_{\sigma i} e_{\sigma i} f_{\sigma i}^0 \tag{3.49}$$

Similarly, the equations of second order can be obtained by taking the moments of Eq. (3.46).

$$\partial_{t_1} \rho = 0 \tag{3.50}$$

This is the second-order continuity equation.

$$\partial_{t_1} (\rho \mathbf{u}) + \nabla \bullet (1 - \frac{1}{2\tau}) \Pi^1 = 0 \tag{3.51}$$

This is the second-order momentum equation, where Π^1 represents the second-order momentum flux tensor, given by:

$$\Pi^1 = \sum_{\sigma} \sum_{i} e_{\sigma i} e_{\sigma i} f_{\sigma i}^1 \tag{3.52}$$

Now, let us proceed to simplify the momentum flux tensors. By substituting the equilibrium distribution function into the expression for Π^0 , we can get:

$$\Pi^0_{\alpha\beta} = \left[2A_1 + 4A_2 + (4C_2 + 2D_1 + 4D_2)\mathbf{u}^2 \right] \delta_{\alpha\beta} + 8C_2 u_\alpha u_\beta + (2C_1 - 8C_2) u_\alpha u_\beta \delta_{\alpha\beta} \tag{3.53}$$

The first term on the right hand side of Eq. (3.53) represents pressure, thus,

$$4C_2 + 2D_1 + 4D_2 = 0 \tag{3.54}$$

Otherwise, we would obtain unphysical velocity-dependent pressure. Also, in order to satisfy Galilean invariance, we need:

$$2C_1 - 8C_2 = 0 \tag{3.55}$$

Thus, Eq. (3.53) can be simplified to:

$$\Pi^0_{\alpha\beta} = (2A_1 + 4A_2)\delta_{\alpha\beta} + 8C_2 u_\alpha u_\beta \tag{3.56}$$

Assuming that (Hou et al. (1995))

$$8C_2 = \rho \tag{3.57}$$

and

$$2A_1 + 4A_2 = c_s^2 \rho \tag{3.58}$$

where c_s is the speed of sound, which will be determined later, we get

$$\Pi^0_{\alpha\beta} = c_s^2 \rho \delta_{\alpha\beta} + \rho u_\alpha u_\beta \tag{3.59}$$

Thus, the first-order momentum equation simplifies to:

$$\partial_{t_0}(\rho \mathbf{u}) + \nabla \bullet (\rho \mathbf{u}\mathbf{u}) = -\nabla(c_s^2 \rho) \tag{3.60}$$

Eqs. (3.47) and (3.60) construct the Euler's equations which are derived from the first-order expansion of the LBE. And the pressure is given by $p = c_s^2 \rho$.

Now let us proceed to derive these equations to the second order of ε, i.e., $O(\varepsilon^2)$. In order to simplify Π^1, we need to find the non-equilibrium part of the distribution function, $f_{\sigma i}^1$. From Eq. (3.45), we can get:

$$f_{\sigma i}^1 = -\tau(\partial_{t_0} f_{\sigma i}^0 + e_{\sigma i} \bullet \nabla f_{\sigma i}^0) \tag{3.61}$$

Substitute Eq. (3.61) into Eq. (3.52), and using the properties of the lattice tensors, we can obtain:

$$\Pi_{\alpha\beta}^1 = -\tau\left\{\partial_{t_0}\left[(c_s^2\rho)\delta_{\alpha\beta} + \rho u_\alpha u_\beta\right] + \partial_\gamma B_1 u_\theta 2\delta_{\alpha\beta\gamma\theta} + \partial_\gamma B_2 u_\theta(4\Delta_{\alpha\beta\gamma\theta} - 8\delta_{\alpha\beta\gamma\theta})\right\}$$

$$= -\tau\left\{-c_s^2\delta_{\alpha\beta}\partial_\gamma(\rho u_\gamma) + \partial_{t_0}(\rho u_\alpha u_\beta) + \partial_\alpha(2B_1 - 8B_2)u_\beta\delta_{\alpha\beta} + 4\partial_\gamma(B_2 u_\gamma)\delta_{\alpha\beta} + 4\partial_\alpha(B_2 u_\beta) + 4\partial_\beta(B_2 u_\alpha)\right\} \tag{3.62}$$

To maintain isotropy, setting:

$$2B_1 - 8B_2 = 0 \tag{3.63}$$

Incorporating Eqs. (3.42c) and (3.63), the coefficients can be uniquely determined:

$$B_1 = \frac{\rho}{3} \tag{3.64a}$$

$$B_2 = \frac{\rho}{12} \tag{3.64b}$$

Then Eq. (3.62) becomes:

$$\Pi_{\alpha\beta}^1 = -\tau\left\{\frac{1}{3}\delta_{\alpha\beta}\partial_\gamma(\rho u_\gamma) - c_s^2\partial_\gamma(\rho u_\gamma)\delta_{\alpha\beta} + \frac{1}{3}\partial_\alpha(\rho u_\beta) + \frac{1}{3}\partial_\beta(\rho u_\alpha) + \partial_{t_0}(\rho u_\alpha u_\beta)\right\} \tag{3.65}$$

The time derivative term in the above equation could be simplified by Eqs. (3.47) and (3.60):

$$\partial_{t_0}(\rho u_\alpha u_\beta) = -u_\alpha\partial_\beta(c_s^2\rho) - u_\beta\partial_\alpha(c_s^2\rho) - \partial_\gamma(\rho u_\alpha u_\beta u_\gamma) \tag{3.66}$$

Eq. (3.65) becomes:

$$\Pi^1_{\alpha\beta} = -\tau\left\{(\frac{1}{3}-c_s^2)\delta_{\alpha\beta}\partial_\gamma(\rho u_\gamma)+\frac{1}{3}\partial_\alpha(\rho u_\beta)+\frac{1}{3}\partial_\beta(\rho u_\alpha)-u_\alpha\partial_\beta(c_s^2\rho)-u_\beta\partial_\alpha(c_s^2\rho)-\partial_\gamma(\rho u_\alpha u_\beta u_\gamma)\right\} \tag{3.67}$$

Since LBE and the associated equilibrium distribution functions is valid only for small velocities, we neglect terms of the order of $O(u^3)$ in the above equation, we obtain:

$$\Pi^1_{\alpha\beta} = -\tau\left\{(\frac{1}{3}-c_s^2)\delta_{\alpha\beta}\partial_\gamma(\rho u_\gamma)+\frac{1}{3}\partial_\alpha(\rho u_\beta)+\frac{1}{3}\partial_\beta(\rho u_\alpha)-u_\alpha\partial_\beta(c_s^2\rho)-u_\beta\partial_\alpha(c_s^2\rho)\right\}+O(u^3) \tag{3.68}$$

Finally, we get the continuity equation:

$$\partial_t\rho+\nabla\bullet(\rho\mathbf{u})=0 \tag{3.69}$$

Momentum equation:

$$\partial_t(\rho u_\alpha)+\partial_\beta(\rho u_\alpha u_\beta) = -\partial_\alpha(c_s^2\rho)+\varepsilon\left\{\partial_\alpha\left[(\tau-\frac{1}{2})(\frac{1}{3}-c_s^2)\partial_\gamma(\rho u_\gamma)\right]\right.$$

$$\left.+\partial_\beta(\tau-\frac{1}{2})\left[\frac{1}{3}\rho(\partial_\alpha u_\beta+\partial_\beta u_\alpha)+(\frac{1}{3}-c_s^2)(u_\alpha\partial_\beta\rho+u_\beta\partial_\alpha\rho)\right]\right\}+O(u^3)+O(\varepsilon^3) \tag{3.70}$$

The above equation can be significantly simplified is we set the speed of sound:

$$c_s^2=\frac{1}{3} \tag{3.71}$$

This tactic provides us the speed of sound in the LBM framework. Thus, the momentum equation becomes:

$$\partial_t(\rho u_\alpha)+\partial_\beta(\rho u_\alpha u_\beta) = -\partial_\alpha(c_s^2\rho)+\partial_\beta(2\nu\rho S_{\alpha\beta})+O(u^3)+O(\varepsilon^3) \tag{3.72}$$

where $S_{\alpha\beta}$ is the strain rate tensor, defined as:

$$S_{\alpha\beta} = \frac{1}{2}(\partial_\alpha u_\beta + \partial_\beta u_\alpha) \tag{3.73}$$

Also, assume that the kinematic viscosity is defined as:

$$\nu = \frac{2\tau - 1}{6}\delta_t \tag{3.74}$$

With the pressure $p = c_s^2 \rho$, we can get:

$$\partial_t(\rho u_\alpha) + \partial_\beta(\rho u_\alpha u_\beta) = -\partial_\alpha p + \partial_\beta(2\nu\rho S_{\alpha\beta}) + O(u^3) + O(\varepsilon^3) \tag{3.75}$$

Neglecting all the terms of the order of $O(u^3)$ and $O(\varepsilon^3)$, finally, we get the momentum equation:

$$\partial_t(\rho u_\alpha) + \partial_\beta(\rho u_\alpha u_\beta) = -\partial_\alpha p + \partial_\beta(2\mu S_{\alpha\beta}) \tag{3.76}$$

which is the Navier-Stokes momentum equation.

3.4 Single phase LBM benchmark test

To test the applicability of LBM, single phase flow is first simulated and compared to the analytical solutions. Only few analytical solutions of Navier-Stokes equations are known. One of them is the plane Poiseuille flow in a channel of height H where the flow is steady. For this fully developed 2-D channel flow driven by constant pressure gradient, the analytical solution is given as follows:

$$u_{exact}(y) = -\frac{1}{2}\frac{dp}{dx}\frac{H^2}{\rho\nu}\left[(\frac{y}{H})^2 - \frac{y}{H}\right] \tag{3.77}$$

where $\frac{dp}{dx}$ is the constant pressure gradient, ν is the kinematic viscosity, 'x' is along the flow direction, 'y' is the vertical direction.

In order to evaluate the computational error of the model, the following relative error is defined:

$$E = \frac{\sum_j \left| u_{LBM}(j) - u_{exact}(j) \right|}{\sum_j \left| u_{exact}(j) \right|} \tag{3.78}$$

The grid size for the 2-D channel is fixed at 51×51. The periodic boundary condition is imposed on the left and right side of the domain, the rigid wall boundary condition is imposed on the top and bottom of the domain. Two different wall boundary conditions are used: half-way bounce back and extrapolation scheme proposed by Chen et al. (1996).

3.4.1 Boundary conditions

Periodic boundary conditions are most desired due to its simplicity. The term 'periodic' is self-explanatory in the way the boundary works, i.e., all the particle distribution functions leaving the domain exit will enter the inlet from the direction they leave, and it will apply for the inlet particle distribution function in the same way.

To generate a non-slip wall boundary condition, the 'bounce-back' boundary condition was first proposed. This concept was borrowed from LGA, where the particles will be bounced back opposite to the direction in which it hits the wall. However, this bounce-back technique only gives first order accuracy, while the LBE is second order accurate. Thus, errors will be

propagated from the wall boundary into the fluids. Later, Ziegler (1993) proposed a half-way bounce back scheme for the non-slip wall boundary condition. In their scheme, the wall was placed half way between the fluid nodes and the imaginary nodes, which are used to bounce back the particle distribution functions streaming out of the wall. In this manner, they acquired second order accuracy for the boundary condition.

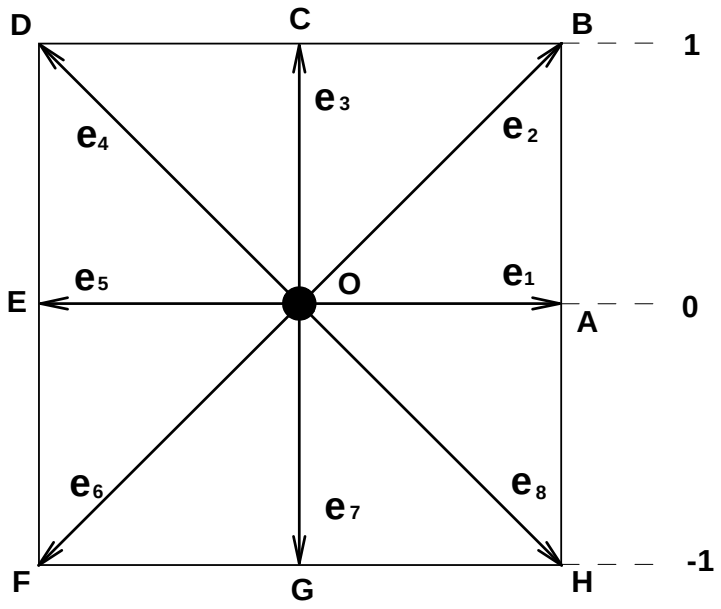

Figure 7: The schematic view of extrapolation boundary condition.

Later, Chen et al. (1996) proposed an extrapolation scheme for the non-slip wall boundary condition, which is also second order accurate. The idea of this scheme is very simple: they assume there is one additional layer beyond the wall boundary, as shown in Figure 7. In Figure 7, the layer labeled with '0' represents the wall, '-1' represents the additional layer and '1'

represents the first layer inside the fluid. To calculate the particle distribution functions streaming out of the wall, the following equation is employed:

$$f_i^0 = \frac{f_i^{-1} + f_i^1}{2} \tag{3.79}$$

where f_i^{-1}, f_i^0 and f_i^1 are the particle distribution functions on the outside layer, the wall layer, and the first layer inside the fluid, respectively.

3.4.2 Results

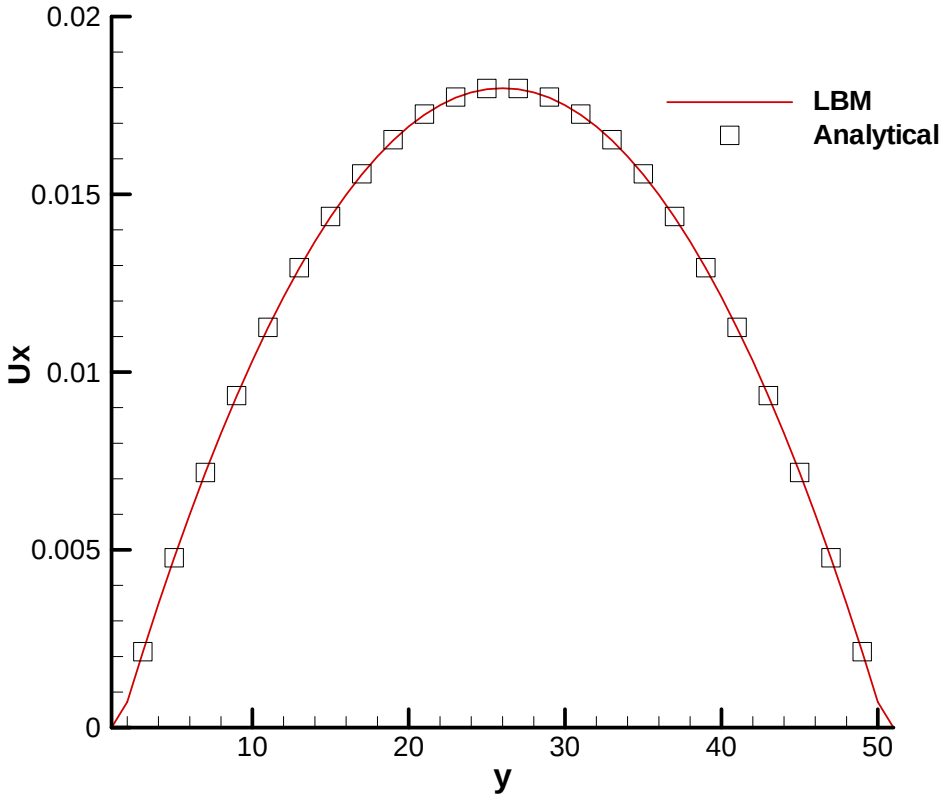

Figure 8: Both LBM and analytical velocity profiles at the outlet for a fully developed pressure driven flow in a 2-D channel with the height of 51 in LBM units are compared, the pressure gradient is set to be 10^{-5}, $\tau = 1.0$, half-way bounce back wall boundary condition is used for LBM simulation.

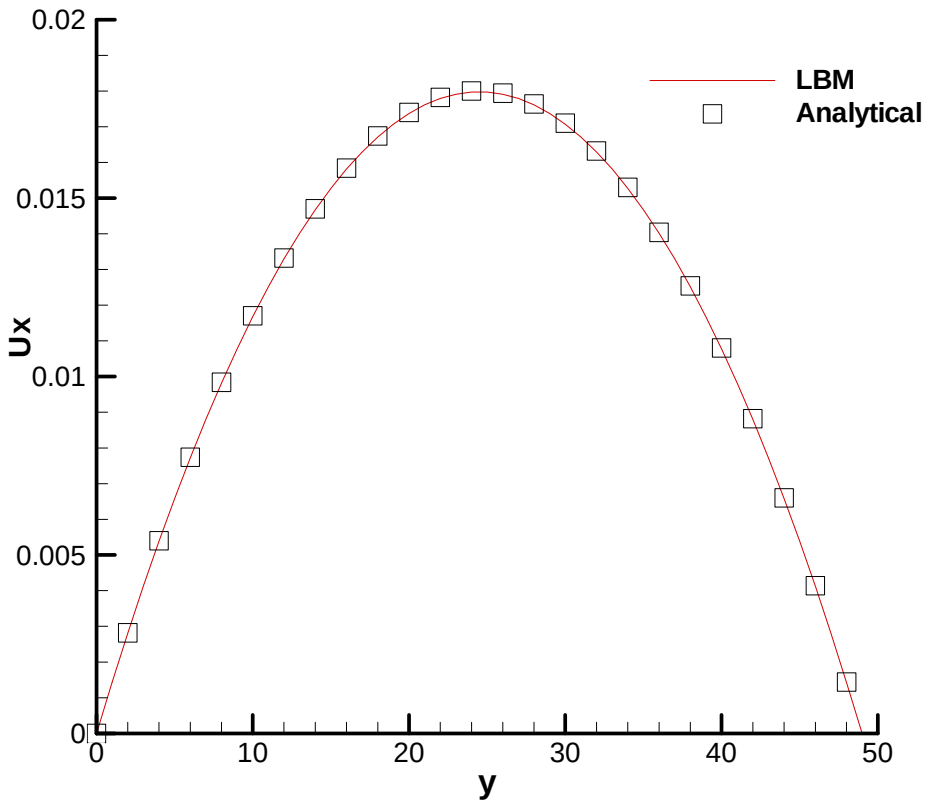

Figure 9: Both LBM and analytical velocity profiles at the outlet for a fully developed pressure driven flow in a 2-D channel with the height of 51 in LBM units are compared, the pressure gradient is set to be 10^{-5}, $\tau = 1.0$, extrapolation wall boundary condition is used for LBM simulation.

From Figure 8 and Figure 9, where the relaxation time is set to be unity, excellent matches between the LBM simulation results and the analytical solution are found. In Figure 10, the LBM simulation results are compared with the analytical solution at different relaxation times. In Table 3, the relative errors are computed for both half-way bounce and extrapolation schemes. For relaxation time in the range of $0.8 < \tau < 4.0$, the LBM results are found to be acceptable.

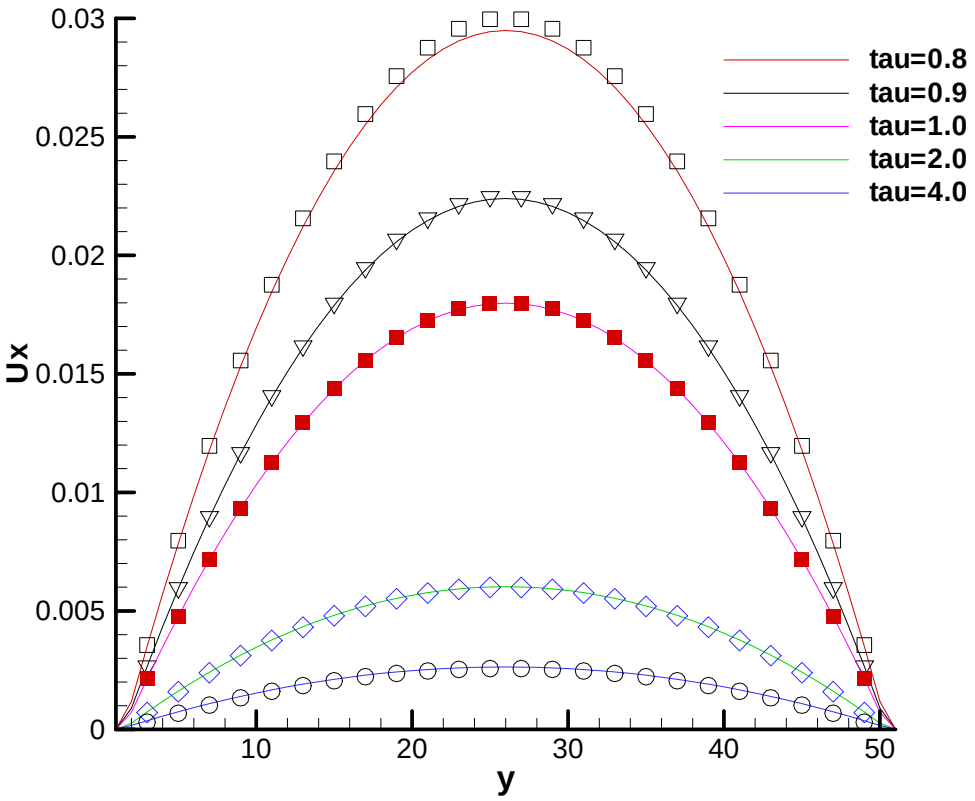

Figure 10: Both LBM and analytical velocity profiles at the outlet for a fully developed pressure driven flow in a 2-D channel with the height of 51 in LBM units are compared, the pressure gradient is set to be 10^{-5}, $0.8 < \tau < 4.0$, half-way bounce back wall boundary condition is used for LBM simulations.

Table 3: Relative errors for two different boundary conditions are different τ values

τ	0.7	0.8	0.9	1.0	2.0	4.0	10.0
Half-way	6.66%	1.94%	0.72%	0.38%	0.74%	3.89%	29.3%
Extrapolation	6.52%	1.77%	0.53%	0.13%	0.076%	0.96%	11.6%

CHAPTER FOUR: MULTIPHASE LBE AND BENCHMARK TESTS

4.1 Review of existing multiphase LBM schemes

4.1.1 Chromodynamic model

Gunstensen et al. (1991) were the first to develop a multiphase LBM method. Their model was developed from the two-component LG model proposed by Rothman & Keller (1988). In their model, there are two particle distribution functions, red-colored and blue-colored particles, which represent two different kinds of fluids. To maintain interfaces and to separate different phases, a "recoloring" process was introduced to enforce the colored fluids to move toward fluids of the same kind. Thus, this method is also called chromodynamic model. And during this "recoloring" process, the conservation laws are strictly imposed. It has been used in a number of applications, such as flow through porous media, Rayleigh-Taylor instability and so on. However, this method has two main drawbacks. First, the "recoloring" process is artificial and does not have a sound physical background. Thus, this perturbation step involving the color redistribution results in artificial anisotropic surface tension which induces unphysical velocity currents at the interface. Second, the "recoloring" process requires time-consuming computations for the local maxima. In addition, another drawback of the original chromodynamic model is that the density and viscosity of two fluids must be the same. Later, Grunau et al (1993) modified this model to allow the variations of density and viscosity.

4.1.2 Pseudo-potential model

Shan & Chen (1993) proposed a pseudo-potential LBM model using a non-local interaction between particles at neighboring lattice sites. This additional force at each lattice site was employed to approximate the effects of the microscopic level of molecular interactions. Although it can be shown that the total momentum is conserved over the whole computational domain, the momentum is not locally conserved because of these non-local interactions. As a result, a spurious velocity field always exists at the interface. In Shan-Chen's model, different equation of state (EOS) will be formed by using different interaction potentials, and phase separation occurs automatically when interaction potentials are properly chosen. Yuan & Laura (2006) presented a summary of a few different EOS by using different interaction potentials to compare the spurious currents, density ratio of two fluids, and temperature range. Although this method has several drawbacks, it has been used for a wide range of problems (Shan & Doolen (1995); Sankaranarayanan et al. (1999)). Since the collision model in the original Shan-Chen's method is explicit, Sankaranarayanan et al. (2002) proposed an implicit collision formulation to allow the change of viscosity in a much wider range. Thus, a very broad range of Morton number and Eotvos number were obtained to simulate the rise behavior of a single bubble and multiple bubbles.

4.1.3 Free energy model

Instead of using interaction potential between the computational particles, Swift et al. (1995, 1996) developed a two-phase LBM model based on a thermodynamic approach. They introduced a bulk Helmholtz free energy per unit volume, which made the equation of state for the two

phases as an outset. Thus, Swift's LBM model was usually known as free energy model in LBM. However, there were serious problems with non-Galilean invariant terms that were associated with density variations in the liquid-gas two phase system. Later, Inamuro et al. (2000) modified Swift's model to by applying a so-called asymptotic theory, and obtained a Galilean-invariant model. They demonstrated drop deformation and break-up in a shear flow by using this model. The advantage of the thermodynamically based free energy model is that it is straightforward to incorporate surface tension, and this allows better parametric control for the simulations.

4.1.4 HSD model

He, Shan, and Doolen (HSD) (1998) proposed a novel LBE formulation for non-ideal gases based on the continuous discrete Boltzmann equation (DBE), in which the interfacial dynamics are modeled by incorporating molecular interactions. The collision term in lattice Boltzmann equation can be well modeled by Enskog's theory for short-range molecular interaction and the mean-field approximation for long range molecular interaction. Later, He et al. (1999) themselves extended the HSD model to be able to simulate incompressible multiphase flow. In this extended model, two distribution functions are employed. The first distribution function is used to calculate the pressure and velocity fields, while the other one is used only to locate the interface.

4.2 Formulations of multiphase LBE and boundary condition

4.2.1 Multiphase LBE

In this study, the fifteen-velocity model for three-dimensions (D3Q15) proposed by Inamuro et al. (2004) has been implemented. The velocity vectors in this model are given by (see Figure 11):

$$\begin{aligned}&\left[e_1, e_2, e_3, e_4, e_5, e_6, e_7, e_8, e_9, e_{10}, e_{11}, e_{12}, e_{13}, e_{14}, e_{15}\right] \\ &= \begin{bmatrix} 0 & 1 & 0 & 0 & -1 & 0 & 0 & 1 & -1 & 1 & 1 & -1 & 1 & -1 & -1 \\ 0 & 0 & 1 & 0 & 0 & -1 & 0 & 1 & 1 & -1 & 1 & -1 & -1 & 1 & -1 \\ 0 & 0 & 0 & 1 & 0 & 0 & -1 & 1 & 1 & 1 & -1 & -1 & -1 & -1 & 1 \end{bmatrix}\end{aligned} \tag{4.1}$$

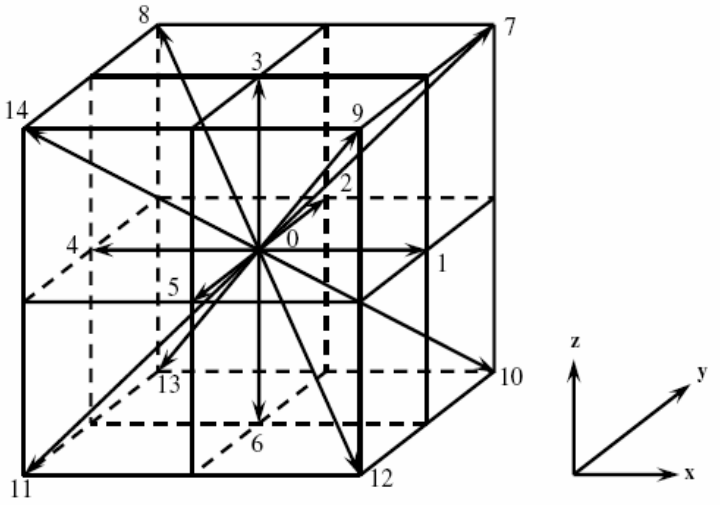

Figure 11: Discrete velocity vectors for D3Q15 lattice Boltzmann model

In the present method, two-phase fluid flow simulations have been carried out for a purely isothermal system. Two particle distribution functions, f_i and g_i, have been introduced. The Function f_i is used to calculate the order parameter, ϕ, which distinguishes the two phases, while g_i is used to calculate a predicted velocity, $\mathbf{u}^*$, of the two-phase fluids without a pressure

gradient. The evolution of the particle distribution functions $f_i(\mathbf{x},t)$ and $g_i(\mathbf{x},t)$ with particle velocity $\mathbf{e}_i$ at the point $\mathbf{x}$ and time t is carried out by the following equations:

$$f_i(\mathbf{x}+\mathbf{e}_i\Delta t, t+\Delta t) = f_i(\mathbf{x},t) - \frac{f_i(\mathbf{x},t) - f_i^{eq}(\mathbf{x},t)}{\tau_f} \tag{4.2}$$

$$g_i(\mathbf{x}+\mathbf{e}_i\Delta t, t+\Delta t) = g_i(\mathbf{x},t) - \frac{g_i(\mathbf{x},t) - g_i^{eq}(\mathbf{x},t)}{\tau_g} + 3E_i\mathbf{e}_{i\alpha}\frac{1}{\rho}\left[\frac{\partial}{\partial x_\beta}\left\{\mu\left(\frac{\partial \mathbf{u}_\beta}{\partial x_\alpha} + \frac{\partial \mathbf{u}_\alpha}{\partial x_\beta}\right)\right\}\right]\Delta x \tag{4.3}$$

where τ_f and τ_g are the single relaxation time parameters for the two particle distribution functions f_i and g_i respectively, Δx is the unit spacing of the cubic lattice and Δt is the time step for the particles to travel through the lattice spacing. The last term in Eq. (4.3) represents the viscous stress tensor. f_i^{eq} and g_i^{eq} are the modified particle equilibrium distributions for this heuristic two-phase model chosen in order to satisfy the desired evolution equations as is shown below.

The macroscopic variables, order parameter ϕ and the predicted velocity of two-phase fluids $\mathbf{u}^*$ are given from the moments of the functions f_i and g_i at each location, and are given as:

$$\phi = \sum_{i=1}^{15} f_i \tag{4.4}$$

$$\mathbf{u}^* = \sum_{i=1}^{15} \mathbf{e}_i g_i \tag{4.5}$$

The equilibrium functions f_i^{eq} and g_i^{eq} are given by:

$$f_i^{eq} = H_i\phi + F_i\left[p_0 - \kappa_f \phi \frac{\partial^2 \phi}{\partial x_\alpha{}^2} - \frac{\kappa_f}{6}(\frac{\partial \phi}{\partial x_\alpha})^2 \right] + 3E_i\phi e_{i\alpha}u_\alpha + E_i\kappa_f G_{\alpha\beta}(\phi)e_{i\alpha}e_{i\beta} \tag{4.6}$$

$$\begin{aligned} g_i^{eq} &= E_i\left[1 + 3e_{i\alpha}u_\alpha - \frac{3}{2}u_\alpha u_\alpha + \frac{9}{2}e_{i\alpha}e_{i\beta}u_\alpha u_\beta + \frac{3}{2}(\tau_g - \frac{1}{2})(\frac{\partial u_\beta}{\partial x_\alpha} + \frac{\partial u_\alpha}{\partial x_\beta})e_{i\alpha}e_{i\beta} \right] \\ &+ E_i\frac{\kappa_g}{\rho}G_{\alpha\beta}(\rho)e_{i\alpha}e_{i\beta} - \frac{2}{3}F_i\frac{\kappa_g}{\rho}(\frac{\partial \rho}{\partial x_\alpha})^2 \end{aligned} \tag{4.7}$$

where

$$\mathrm{E_i} = \begin{cases} 2/9, & i=1, \\ 1/9, & i=1,...,7 \\ 1/72, & i=8,...,15 \end{cases}, \quad F_i = \begin{cases} -7/3, & i=1, \\ 1/3, & i=1,...,7 \\ 1/24, & i=8,...,15 \end{cases}, \quad H_i = \begin{cases} 1, & i=1, \\ 0, & i=1,...,15 \end{cases} \tag{4.8}$$

and

$$G_{\alpha\beta}(\phi) = \frac{9}{2}\frac{\partial \phi}{\partial x_\alpha}\frac{\partial \phi}{\partial x_\beta} - \frac{3}{2}\frac{\partial \phi}{\partial x_\gamma}\frac{\partial \phi}{\partial x_\gamma}\delta_{\alpha\beta} \tag{4.9}$$

where κ_f is the surface tension parameter specified to control the width of the interface between two phases, while κ_g controls the strength of the surface tension, and p_0 is the thermodynamic pressure, given by

$$p_0 = \phi\frac{\partial \psi}{\partial \phi} - \psi = \phi T\frac{1}{1-b\phi} - a\phi^2 \tag{4.10}$$

with

$$\psi(\phi, T) = \phi T In(\frac{\phi}{1-b\phi}) - a\phi^2 \tag{4.11}$$

where $\psi(\phi, T)$ is the bulk free energy density. a, b and T are free parameters that can be chosen appropriately.

The first derivatives and laplacian operators ($\partial\phi/\partial x_\alpha$, $\partial\rho/\partial x_\alpha$, $\partial u_\beta/\partial x_\alpha$, $\nabla^2\phi$ and $\nabla^2 u_\alpha$) are calculated using the finite difference approximations in lattice Boltzmann construction and involves the effects from all neighboring nodes, given as:

$$\frac{\partial\lambda}{\partial x_\alpha} \approx \frac{1}{10}\sum_{i=2}^{15} e_{i\alpha}\lambda(\mathbf{x}+\mathbf{e}_i\delta t) \tag{4.12}$$

$$\nabla^2\lambda \approx \frac{1}{5}\left[\sum_{i=2}^{15}\lambda(\mathbf{x}+\mathbf{e}_i\delta t) - 14\lambda(x)\right] \tag{4.13}$$

Once the order parameter is determined from the zeroth order moment of the distribution function f_i, the density at the interface is then calculated by:

$$\rho = \begin{cases} \rho_G & \phi < \phi_G^* \\ \dfrac{\Delta\rho}{2}\left[\sin\left(\dfrac{\phi-\overline{\phi^*}}{\Delta\phi^*}\pi\right)+1\right]+\rho_G & \phi_G^* \le \phi \le \phi_L^* \\ \rho_L & \phi > \phi_L^* \end{cases} \tag{4.14}$$

where $\Delta\rho = \rho_L - \rho_G$, $\Delta\phi^* = \phi_L^* - \phi_G^*$, $\overline{\phi^*} = \dfrac{\phi_L^* + \phi_G^*}{2}$. ρ_L and ρ_G are the densities of the bulk liquid and gas phases, respectively. It is important to introduce the cut-off values of the order parameters, ϕ_L^* and ϕ_G^*, as the maximum and minimum values of the order parameter ϕ are changed slightly from their initial values during the simulation. These cut-off values help to keep the density of each phase at constant values during the entire simulation duration.

The dynamic viscosity for the two phases across the interface is computed based on a linear interpolation as:

$$\mu = \frac{\rho-\rho_G}{\rho_L-\rho_G}(\mu_L-\mu_G)+\mu_G \tag{4.15}$$

where μ_L and μ_G are the dynamic viscosity of liquid and gas phases, respectively.

The surface tension σ between the liquid and gas phases is given by:

$$\sigma = \kappa_g \int_{-\infty}^{\infty} (\frac{\partial \rho}{\partial \xi})^2 d\xi \tag{4.16}$$

where ξ is the direction normal to the interface. In all the simulations carried out in the present study, the surface tension σ is calculated as a post-processing value after conducting static droplet tests. σ is numerically integrated along the interface after the two phases have been equilibrated. The predicted velocity given by $\mathbf{u}^*$ is not divergence free, since it is derived based on a flow without a pressure gradient. To acquire the correct velocity field, the following corrections are incorporated:

$$\mathbf{u} - \mathbf{u}^* = -\frac{\nabla p}{\rho} \tag{4.17}$$

$$\nabla \cdot (\frac{\nabla p}{\rho}) = \nabla \cdot \mathbf{u}^* \tag{4.18}$$

where 'p' is the pressure of the two-phase fluid, which is obtained by solving Eq. (4.19) in the following LBM framework:

$$h_i^{n+1}(\mathbf{x} + \mathbf{e}_i \Delta t) = h_i^n(\mathbf{x}) - \frac{1}{\tau_h}\left[h_i^n(\mathbf{x}) - E_i p^n(\mathbf{x})\right] - \frac{1}{3} E_i \frac{\partial \mathbf{u}_\alpha^*}{\partial x_\alpha} \Delta x \tag{4.19}$$

where the superscript 'n' represents the number of iterations and $\tau_h = \frac{1}{\rho} + \frac{1}{2}$ is the relaxation time for particle distribution function h_i used to update the pressure field. The moment of the distribution function h_i yields the pressure field as:

$$p = \sum_{i=1}^{15} h_i \tag{4.20}$$

The system of Eqs (4.17)-(4.20) is solved until the following convergence criteria are satisfied:

$$\left| p^{n+1} - p^n \right| / \rho < \varepsilon \tag{4.21}$$

4.2.2 Novel treatment for the wetting boundary condition

When a liquid-gas interface meets a solid surface, an angle is formed between the interface and the surface. This angle, which is measured in the liquid, is called the static contact angle, θ_w. According to Young's equation:

$$\cos\theta_w = \frac{\sigma_{sg} - \sigma_{sl}}{\sigma} \tag{4.22}$$

where σ_{sg} is the surface tension force between solid and gas, and σ_{sl} is the surface tension force between solid and liquid.

Recently, a novel LBM boundary condition proposed by Briant et al. (2004) enables the static contact angle between the liquid-gas interface and the wall to be controlled in a way consistent with Cahn theory. In their method, the required wetting potential Ω is calculated by choosing a desired wetting property of the solid surface (i.e., the wetting angel θ_w). Then, the derivative of density normal to the wall, $\partial\rho/\partial n$, can be obtained to calculate the equilibrium particle distribution functions on the wall. By doing this, the effect from the input wall wetting characteristics can be transmitted to the interior fluid nodes through the equilibrium particle

distribution functions. Their static droplet simulations showed that the input and post-processed contact angles match accurately.

In the present work, the treatment of the wall boundary condition is similar to Briant's work, but with a minor modification due to a difference in the equation of state. Briant et al. (2004) used a modified van der Waals free-energy function that enables the surface tension force to be an input parameter. In Inamuro's method (2004), the traditional form of the van der waals free-energy was used, and the surface tension is a post-processed parameter. Therefore, in the current study, instead of specifying an input static contact angle θ_w, an input surface wetting force, η, is used in order to obtain the equilibrium particle distribution functions on the wall. Thus, the first and second derivatives of the order parameter can be treated as shown below:

$$\left.\frac{\partial \phi}{\partial z}\right|_{z=0} = -\eta \tag{4.23}$$

$$\left.\frac{\partial^2 \phi}{\partial z^2}\right|_{z=0} \approx \frac{1}{2}\left(-3\left.\frac{\partial \phi}{\partial z}\right|_{z=0} + 4\left.\frac{\partial \phi}{\partial z}\right|_{z=1} - \left.\frac{\partial \phi}{\partial z}\right|_{z=2}\right) \tag{4.24}$$

where z is the direction perpendicular to the wall. Eq. (4.23) is used to calculate the first term on the right hand side of Eq. (4.24). The second term is calculated by a standard central-difference formula and the third term is calculated by a backward-difference formula taken back into the wall, given by:

$$\left.\frac{\partial \phi}{\partial z}\right|_{z=2} \approx \frac{1}{2}\left(3\phi|_{z=2} - 4\phi|_{z=1} + \phi|_{z=0}\right) \tag{4.25}$$

4.3 Capillary Wave

In this section, the oscillation of a spherical liquid droplet surrounded by gas phase is simulated as a benchmark test to validate the multiphase LBE. For all the simulations, the density ratio between the two phases, $\rho_{\mathrm{L}} / \rho_{\mathrm{G}}$, is fixed at 50 ($\rho_{\mathrm{L}} = 50, \rho_G = 1$). The viscosities of liquid and gas are: $\mu_{\mathrm{L}} = 8\times10^{-3}$, $\mu_G = 1.6\times10^{-4}$. The free parameters are set at: a=1, b=6.7, T=0.035, it follows that $\phi_{\max} = 9.714\times10^{-2}$ and $\phi_{\min} = 1.134\times10^{-2}$. The cut-off values of the order parameter are $\phi_L^* = 9.2\times10^{-2}$ and $\phi_G^* = 1.5\times10^{-2}$. $\kappa_f = 0.5, \tau_f = 1, \tau_g = 1, \varepsilon = 10^{-5}$. The droplet diameter and surface tension are varied. Half of the domain is calculated using the symmetry with y axis. Periodic boundary condition is used on all sides of domain, which has the size of 81×41×81.

The analysis of droplet oscillations is of considerable interest for a wide range of phenomena both in nature and industry, such as the behavior of raindrops and the fluid in biological cells. The surface tension of the droplet acts as a restoring force to maintain its shape in equilibrium. Thus, if small perturbations are imposed to the liquid droplet, the droplet will oscillate to regain an equilibrium state by the capillary force. Suppose the effect of the gravity is neglected, the wave generated by the oscillation process is called capillary wave

Initially, an ellipsoidal droplet is placed in the center of a cubic domain, and the surface of the droplet is given by:

$$\frac{x^2}{(R+0.1R)^2} + \frac{y^2}{(R-0.1R)^2} + \frac{z^2}{(R-0.1R)^2} = 1 \tag{4.26}$$

where R is the radius of the droplet.

The unbalanced surface tension of the ellipsoidal droplet will try to bring the droplet into an equilibrium state. The droplet will encounter an oscillating process and eventually, the droplet will be in spherical shape. The theoretical oscillating frequency of the disturbed droplet when the density of ambient medium is zero is given by (Frohn & Roth (2000)):

$$\omega^2 = \frac{l(l-1)(l+2)}{\bar{r}^3 \rho_L}\sigma \tag{4.27a}$$

where l describes the mode of the oscillation, and $\bar{r}$ is the mean radius of the droplet.

When the density of ambient medium is not zero

$$\omega^2 = \frac{l(l+1)(l-1)(l+2)}{\bar{r}^3 \left[(l+1)\rho_L + l\rho_G\right]}\sigma \tag{4.27b}$$

The oscillating mode of present simulation is 2, as shown from Figure 12-14. From Eqs. (4.27a) and (4.27b), we can get the angular frequency of the oscillation of the droplet is:

$$\omega = \sqrt{\frac{8\sigma}{\bar{r}^3 \rho_L}} \tag{4.28a}$$

$$\omega = \sqrt{\frac{8\sigma}{\bar{r}^3 (\rho_L + \frac{2}{3}\rho_G)}} \tag{4.28b}$$

The difference between these two equations is small for the present case since $\rho_G \ll \rho_L$. Table 4 shows a good comparison of the calculated angular frequencies of the oscillating droplet with the theoretical ones.

Table 4: Comparison of the calculated angular frequencies of the oscillating droplet with the theoretical ones

R	$\bar{r}$	σ	Theoretical	Numerical	Error
15	14.43	0.2	3.262×10^{-3}	3.062×10^{-3}	-6.1%
20	19.25	0.052	1.080×10^{-3}	1.058×10^{-3}	-2.0%
20	19.25	0.186	2.043×10^{-3}	1.982×10^{-3}	-3.0%
20	19.25	0.7	3.964×10^{-3}	3.697×10^{-3}	-6.7%
25	24.06	0.182	1.446×10^{-3}	1.409×10^{-3}	-2.6%

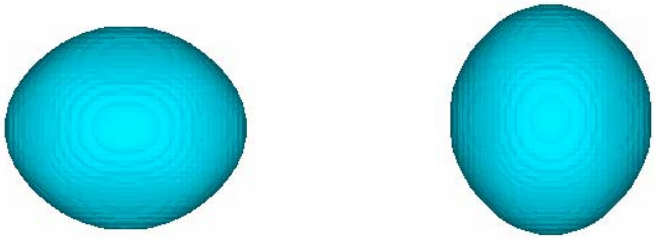

Figure 12: Two extreme states of the two-mode oscillating droplet (3-D view)

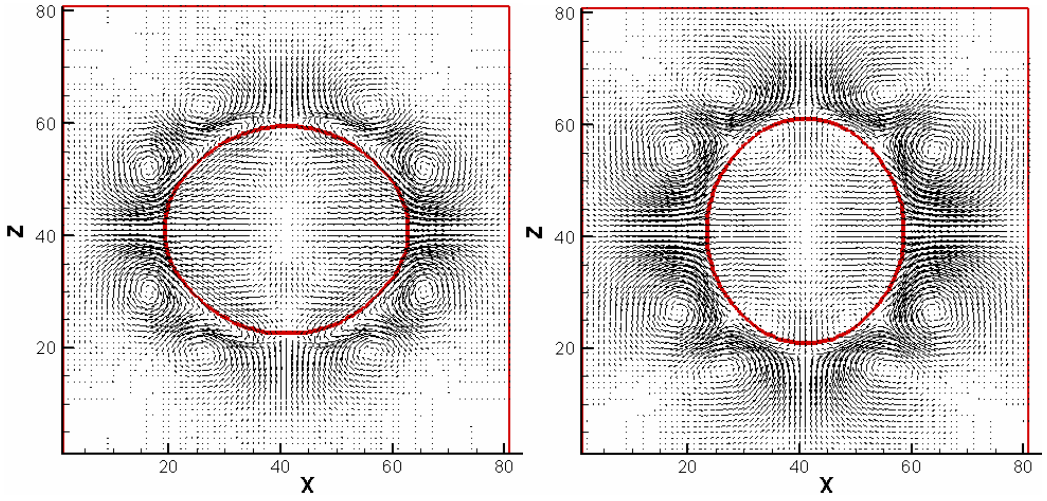

Figure 13: Two extreme states of the two-mode oscillating droplet with the micro-currents generated by the oscillation (2-D view)

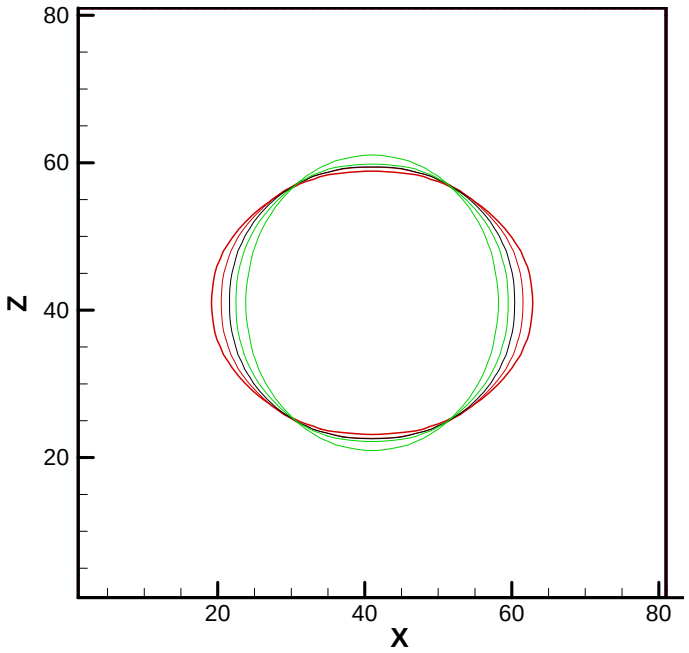

Figure 14: The time evolution of the oscillating droplet shape (Parameters are chosen from the third case of Table 4)

4.4 Binary droplet collisions

In this section, another benchmark test to validate the numerical code, named "binary droplet collisions", are presented and parameters are chosen the same as Inamuro et al. (2004)). Two liquid droplets with the same diameter D are placed a distance 2D apart in the gas phase, and are allowed to move towards each other with a relative collision velocity given by V, as shown in Figure 15. The droplet collision dynamics is described in terms of three important dimensionless parameters: Weber number, Reynolds number, which are given by Eqs. (1.1) and (1.2), and

Impact parameter: $B=\frac{X}{D}$ (4.29)

where X is the vertical distance between the centers of the two droplets (see Figure 14)

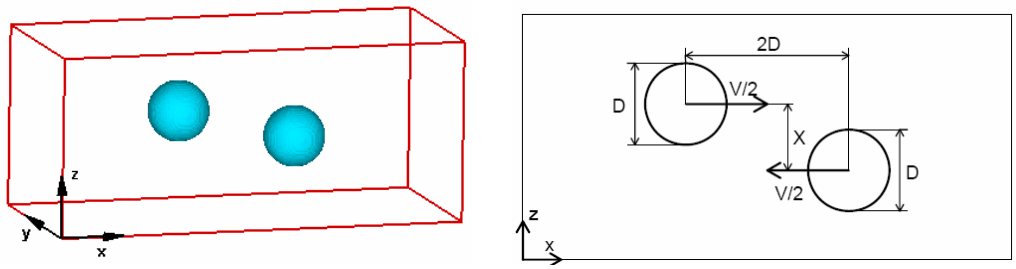

Figure 15: Computational domain for binary droplet collisions (3-D view and 2-D view)

For all the simulations, the density ratio ρ_L / ρ_G, is fixed at 50 ($\rho_L = 50, \rho_G = 1$); The viscosities of liquid and gas are, $\mu_L = 8\times10^{-2}, \mu_G = 1.6\times10^{-3}$. The relative velocity is chosen to be V=0.1. The initial diameter of the spherical droplets is D=32. The Reynolds number is fixed at Re=2000 for all the simulations, while We is varied in the range of 20<We<80 by varying κ_g. Symmetric boundary conditions are employed along the 'y' axis, thereby reducing the computational time in half.

In Figure 16, the time evolution of the binary droplets after collision is shown for We=20, and B=0. The droplet shape represents interface where the mean density, given by $\rho = \frac{\rho_L + \rho_G}{2} = 25.5$, occurs. It can be observed that the two droplets experience small deformation as they approach each other (t^*=1.56). The conjoined droplets reach a maximum elongation in the vertical direction z at t^*=3.13. Subsequently, the extent of deformation decreases, as the surface tension force pulls the droplet to recover its spherical shape. However, the momentum gained by the recoiling motion enables the droplet to form a stretched liquid

cylinder after having reached its maximum deformation in the x direction (t^*=6.25). After some oscillations, this exchange of surface tension energy and momentum is dissipated completely, and the cylinder transforms into a spherical droplet (t^*=23.75). This class of collisions is called the "coalescence collision" (Inamuro et al. (2004)).

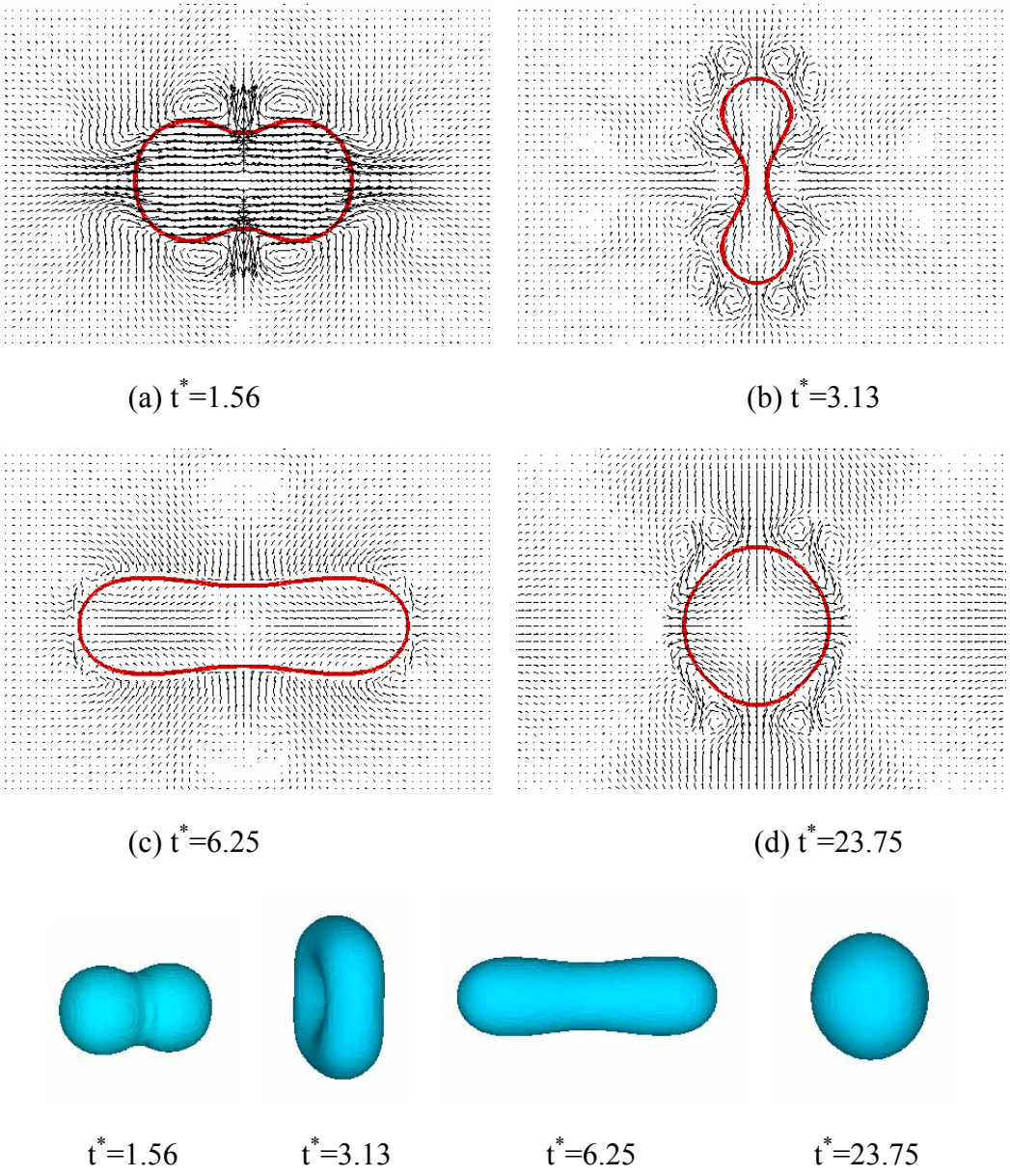

Figure 16: Evolution of droplet shape with time for We=20 and B=0

In Figure 17, the time evolution of the binary droplets collision mechanism is shown for a slightly higher We of 40, and B=0. The droplet interface shown represents $\rho=\frac{\rho_L+\rho_G}{2}=25.5$.

The time evolution of the droplet shape is very similar to the case shown in Figure 16 up to the formation of the long liquid cylinder. However, in this case, the cylinder breaks into two major droplets and a small satellite droplet in the middle (t*=15.0). This type of collision is called the "reflexive separation collision".

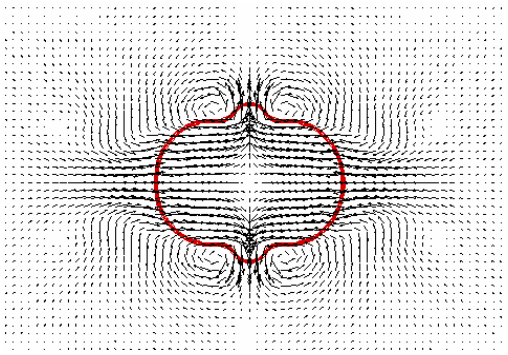

(a) t^*=1.25

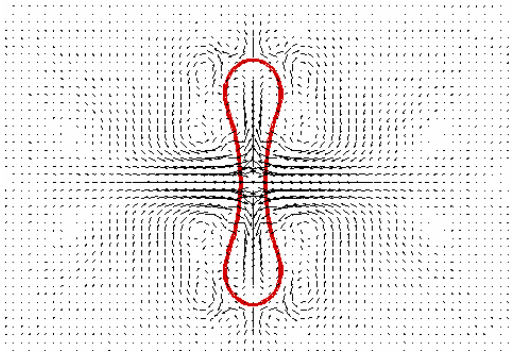

(b) t^*=3.13

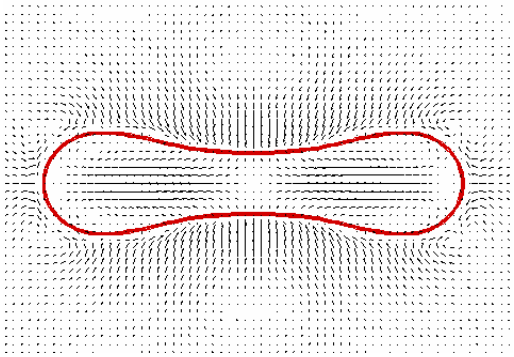

(c) t^*=9.38

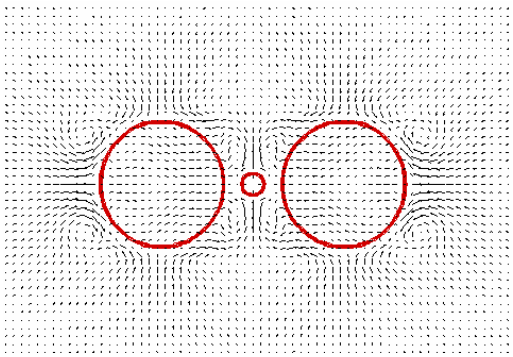

(d) t^*=15.0

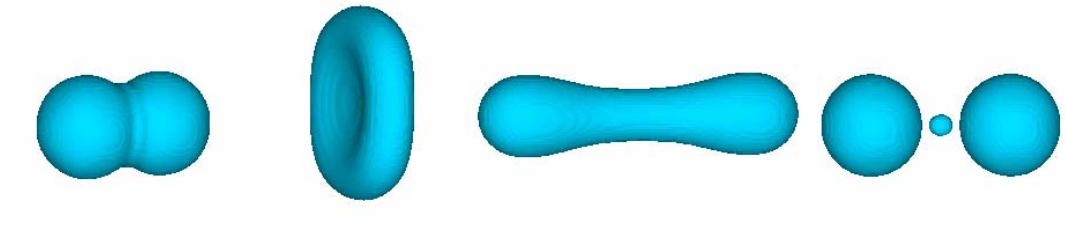

t^*=1.25 t^*=3.13 t^*=9.38 t^*=15.0

Figure 17: Evolution of droplet shape with time for We=40 and B=0

Figure 18 describes the time evolution of the binary droplets collision for a case when We=80, and B=0.5. The two droplets collide at a higher impact parameter, thereby only a small portion of them comes in direct contact with each other. The rest of the portion moves with the initial inertia. Eventually, the conjoined droplet breaks into two major droplets with a small satellite droplet. This type of collision is known as a "stretching separation collision".

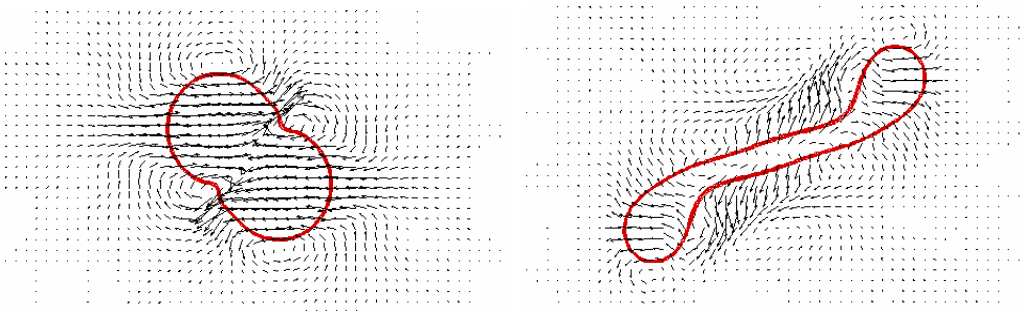

(a) t^*=1.56 (b) t^*=5.0

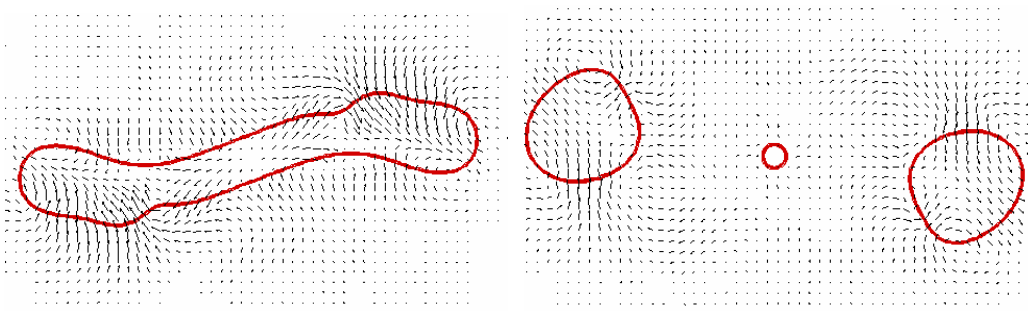

(c) t^*=8.13 (d) t^*=15.0

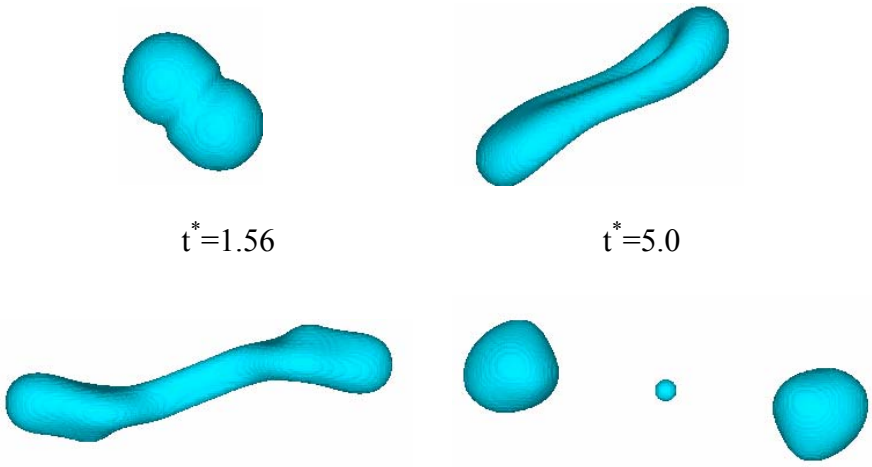

t^*=1.56 t^*=5.0

t^*=8.13 t^*=15.0

Figure 18: Evolution of droplet shape with time for We=80 and B=0.5

CHAPTER FIVE: DROPLET IMPINGEMENT ON A DRY SURFACE

In this chapter, results from the normal impact of a liquid droplet onto a solid, dry surface are reported and discussed. The impact is assumed to be isothermal, and the dry surface is assumed to be perfectly smooth. The physical variables that affect such an impact include: the initial droplet diameter D, impact velocity V, liquid density ρ_L, viscosity μ_L, liquid-gas surface tension σ, and the surface wettability. These variables are grouped into three dimensionless numbers, namely the Weber number, Reynolds numbers and Ohnesorge number, as shown by Eqs. (1.1-1.3). In addition, the spreading characteristics of this dynamic process are captured by measuring the spreading film diameter. This quantity is usually represented by a dimensionless number known as spread factor, d^*, defined by Eq. (1.4). The evolution time, t, is made dimensionless scaled by impact velocity V and the initial spherical drop diameter D, written as:

$$t^* = tV / D \tag{5.1}$$

Usually, the time evolution of spread factor is divided into four phases: the kinematic phase, the spreading phase, the relaxation phase, and the wetting/equilibrium phase (Rioboo et al. (2002)). Figure 19 shows a typical curve for the time evolution of spread factor for We=36 and Re=200 with the equilibrium contact angle θ_w=66.7°. A maximum value of 2.1 for the spread factor is observed at the end of the spreading phase.

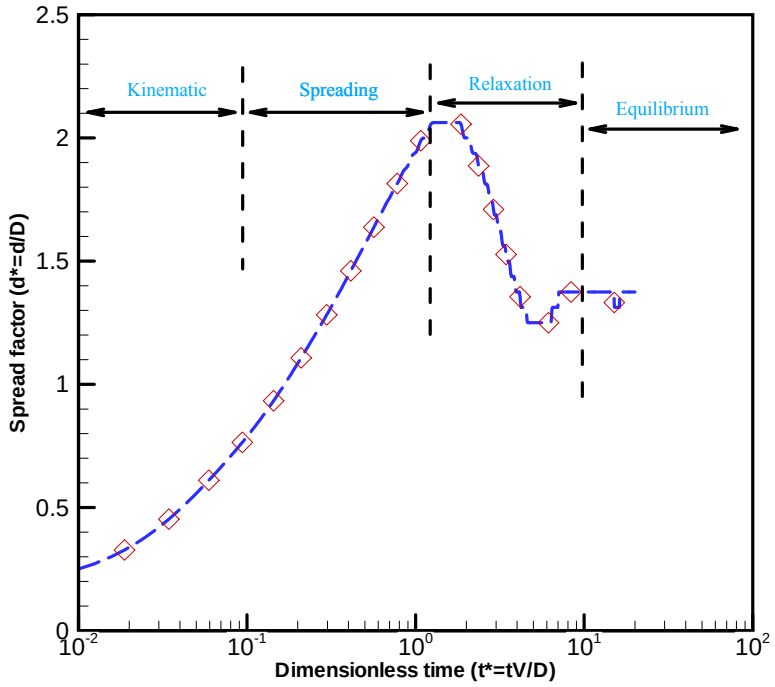

Figure 19: Time evolution of Spread factor showing four distinct phases: kinematic phase, spreading phase, relaxation phase, and equilibrium phase. Data obtained using 3-dimensional LBM simulation for We=36 and Re=200.

5.1 The computational set-up

The three-dimensional computational domain with length L_x, L_y and L_z along the x, y and z axis respectively, and its two-dimensional cross section at $y=L_y/2$ are shown in Figure 20. Periodic boundary condition is used on the sides of the domain (along x and y direction), while no-slip wall boundary condition is used on the top and bottom boundaries of the domain. Using free-slip or open boundary conditions for the top boundary of the domain was found to have little effect on the simulation results presented herein. Due to massive computational requirements of a three-dimensional simulation, only a quarter of the domain is simulated, thereby using symmetry

at x=L_x/2 and y=L_y/2. The domain size for each case is varied according to the initial size of the droplet chosen.

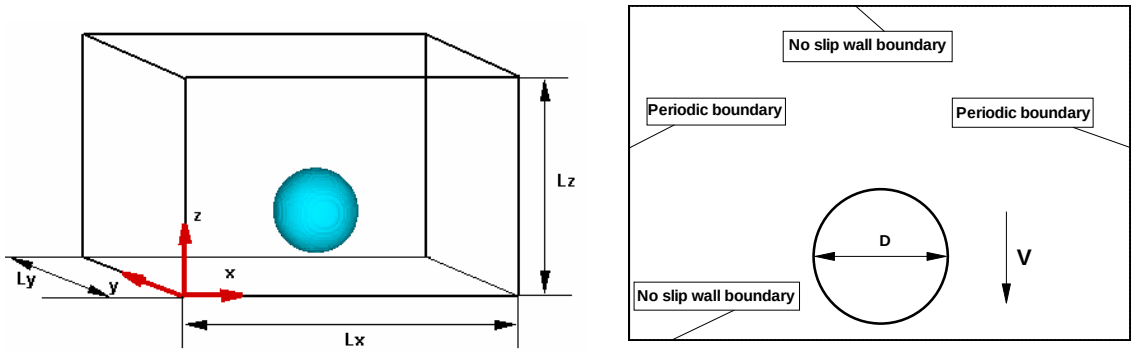

Figure 20: 3-D and 2-D Schematic view of simulation domain for a droplet impingement on a dry surface

Initially, the droplet is placed several nodes away from the surface, and is allowed to equilibrate for 5000 time steps. At this time, the droplet is assigned a uniform velocity V in the vertical direction for about 100 time steps to make sure that the drop attains a steady impact velocity. The viscosity ratio of liquid and gas is fixed at: $\mu_L / \mu_G = 50$. The diameter of the droplet is fixed at D=32. For all other parameters: a=1, b=6.7, T=0.035, it follows that $\phi_{max} = 9.714 \times 10^{-2}$ and $\phi_{min} = 1.134 \times 10^{-2}$. The cut-off values of the order parameter are $\phi_L^* = 9.2 \times 10^{-2}$ and $\phi_G^* = 1.5 \times 10^{-2}$. $\kappa_f = 0.5$, $\tau_f = 1$, $\tau_g = 1$, $\varepsilon = 10^{-5}$. Weber number is varied by changing the parameter κ_g, while Reynolds number is varied by changing liquid viscosity, μ_L.

5.2 Preliminary wetting tests

Even before running a droplet impact case, a preliminary wetting test is conducted to obtain the desired surface wetting characteristic, represented by the static contact angle, θ_w. As an initial condition, half of a spherical droplet is placed at the center of the bottom surface with a specified value for the surface wetting force, depending on whether the surface is hydrophilic, neutral or hydrophobic. This test was allowed to run for 20,000 time steps in order to obtain a stable equilibrium state. Figure 21 shows results for such a test with different wetting behavior, namely, (a) a hydrophilic surface, where $\theta_w=66.7^\circ$ with $\eta=3\times10^{-3}$, (b) a neutral surface, where $\theta_w=90^\circ$ with $\eta=0$, and (c) a hydrophobic surface, where $\theta_w=105^\circ$ with $\eta=-5\times10^{-3}$.

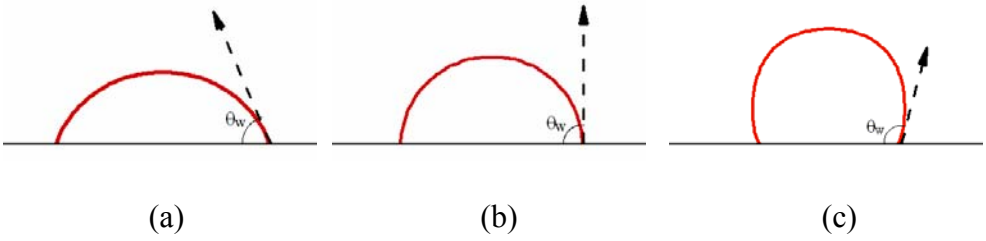

(a) (b) (c)

Figure 21: Preliminary wetting tests for three surfaces: (a) Hydrophilic; (b) Neutral; (c) Hydrophobic

5.3 Validation of power law during Kinematic phase

Figure 22 shows the droplet shape in the kinematic phase defined for the very early stages of impact. During this phase, the spreading droplet represents a truncated sphere without the formation of a spreading lamella along the surface of the wall. According to the geometry shown in Figure 22, we can write the following approximated equation:

$$(d/2)^2 = (D/2)^2 - (D/2 - Vt)^2$$
$$\Rightarrow d = 2\sqrt{DVt - (Vt)^2} \tag{5.2}$$
$$\Rightarrow d^* = 2\sqrt{t^*(1-t^*)}$$

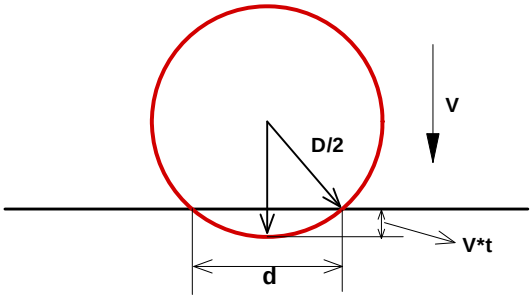

Figure 22: Early stage of impact-Kinematic phase

For small t^*, i.e. $t^* << 1$, Eq. (5.2) indicates that d^* is proportional to $t^{*0.5}$, with an approximate coefficient of 2. Rioboo et al. (2002) obtained a coefficient of 2.8 from numerous experimental data. Figure 23 shows a collection of six cases using the current formulation of LBM, with a curve fit of $d^*=2.5*t^{*0.5}$, in which the coefficient lies between the theoretical prediction and the experimental data. This validation predicts that the droplet spreading factor in the kinematic phase is only a function of the dimensionless time, and does not depend on the physical properties of the fluids involved.

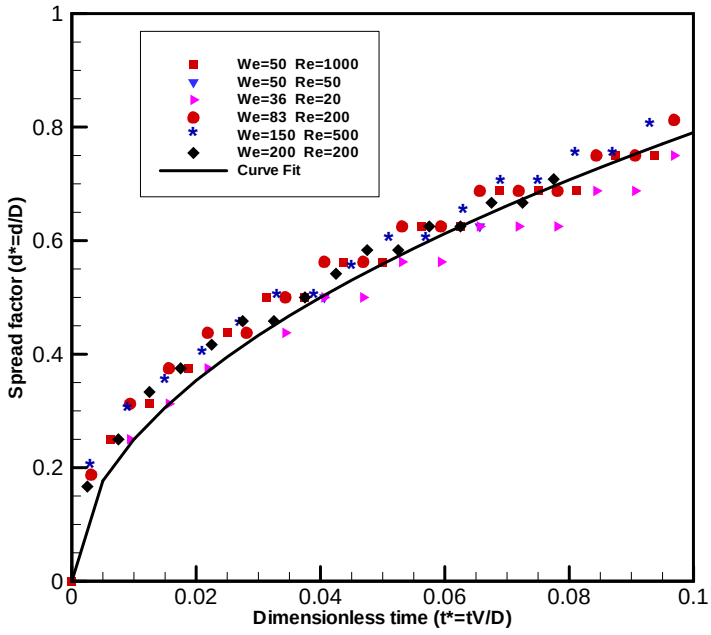

Figure 23: Time evolution of Spread factor during kinematic phase at various Weber and Reynolds numbers, the sold line is the curve fit: d/D=2.5t*0.5

5.4 Simulation observations

After the kinematic phase, all other physical parameters, inertia of impact and surface tension forces begin to play a role to influence the spread factor and the subsequent droplet deformation process. In this section, two different simulation outcomes are shown: deposition and partial rebound.

Figure 24 shows how the droplet deforms with time, and velocity vectors both inside and outside of the droplet are also clearly presented. Weber number is chosen to be 50, the Reynolds number is chosen to be 1000 and the wall has neutral wetting characteristics. The snapshots are taken at different stages of the spreading lamella to show different regimes of the droplet shape. Figure

24(a) shows the droplet deformation at an early stage of impact. During this kinematic phase, the bottom of the spherical droplet is highly squeezed to the sides, thereby producing large velocity currents at the edge of the droplet. The formation of a vortex in the gas phase due to the movement of the droplet in the downward direction can also be observed. Figure 24 (b) shows that a lamella is formed and bounded by a rim when the droplet continues to spread, which reaches its maximum diameter (see Figure 24(b)), indicating the end of the spreading phase. The end of the spreading phase can also be judged by observing the velocity vectors at the edge of the lamella, which almost turn to zero. Figure 24(d-f) shows the rest of the spreading process as the lamella begins to recoil back during the relaxation phase, and eventually reaches its maximum height (see Figure 24(f)). After oscillating for a long time between t^*=6.8 and t^*=23.2, the droplet finally reaches the equilibrium state shown by Figure 24(g), where a half spherical droplet sits on the dry surface. Figure 25 shows the corresponding three-dimensional droplet deformation with time.

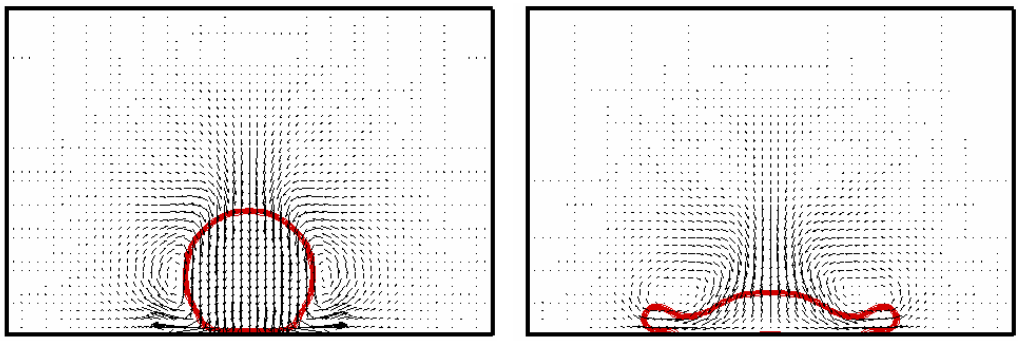

(a) t^*=0.078 (b) t^*=0.86

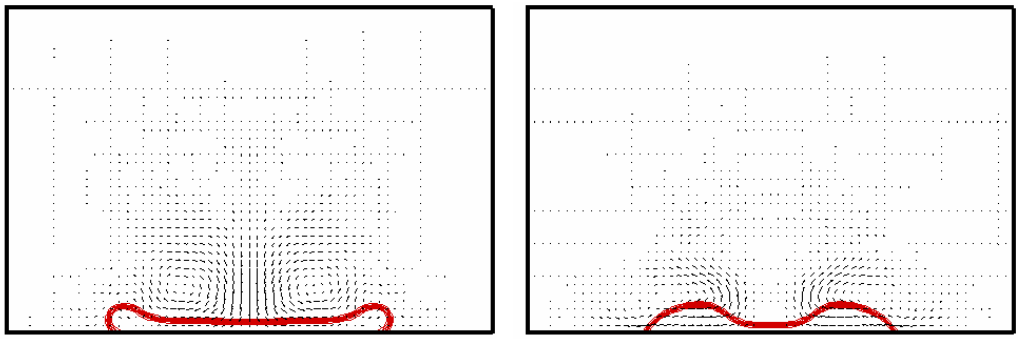

(c) t^*=1.8 (d) t^*=2.9

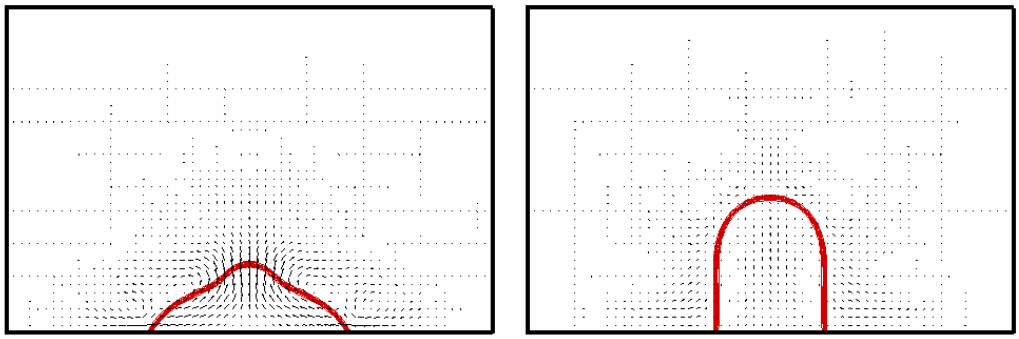

(e) t^*=3.8 (f) t^*=6.8

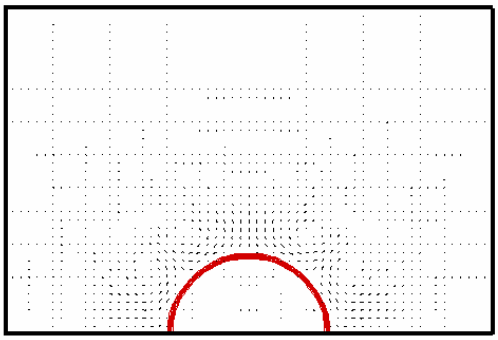

(g) t^*=23.2

Figure 24: 2-D view of the time evolution of droplet shape for We=50, Re=1000.

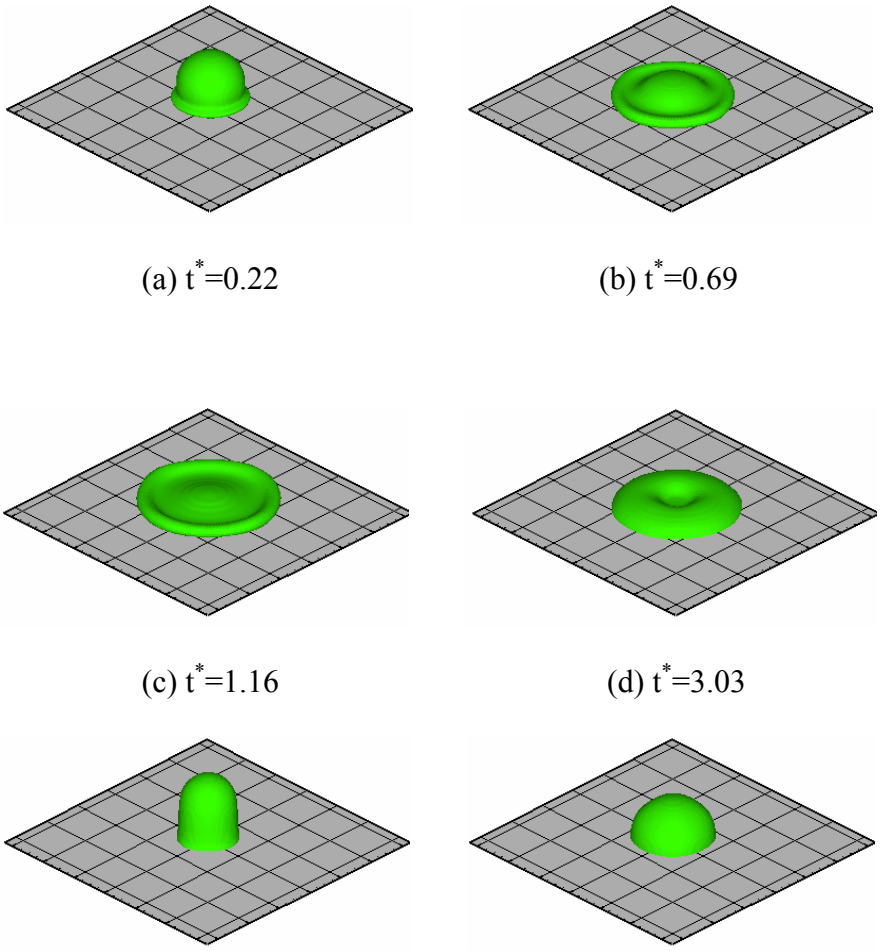

(a) t^*=0.22 (b) t^*=0.69

(c) t^*=1.16 (d) t^*=3.03

(e) t^*=5.84 (f) t^*=23.18

Figure 25: 3-D view of the time evolution of droplet shape for We=50, Re=1000.

In the case given in Figure 25, since the droplet impinges on a neutral wall, it results in a final deposition on the surface although it experiences a long time oscillation induced by the surface tension energy of the droplet. As reported by several researchers [Mao et al. (1997); Rioboo et al. (2002); Mukherjee & Abraham (2007)], droplet at high impact velocity and large surface tension impinges on a super-hydrophobic surface may result in a rebound, meaning completely detachment of the droplet from the surface. In our simulation, as shown in Figure 26, we

observed that the droplet results in a partial rebound on a hydrophobic surface at We=12.5, Re=1000, and $\theta_w = 105^\circ$. This can be seen in Figure 26(f) that the droplet recoils back to the maximum height, with a heavier top and a lighter bottom, where the diameter is less than the original diameter. Further studies are needed to simulate the droplet impingement on super-hydrophobic surface, which may lead to a complete rebound.

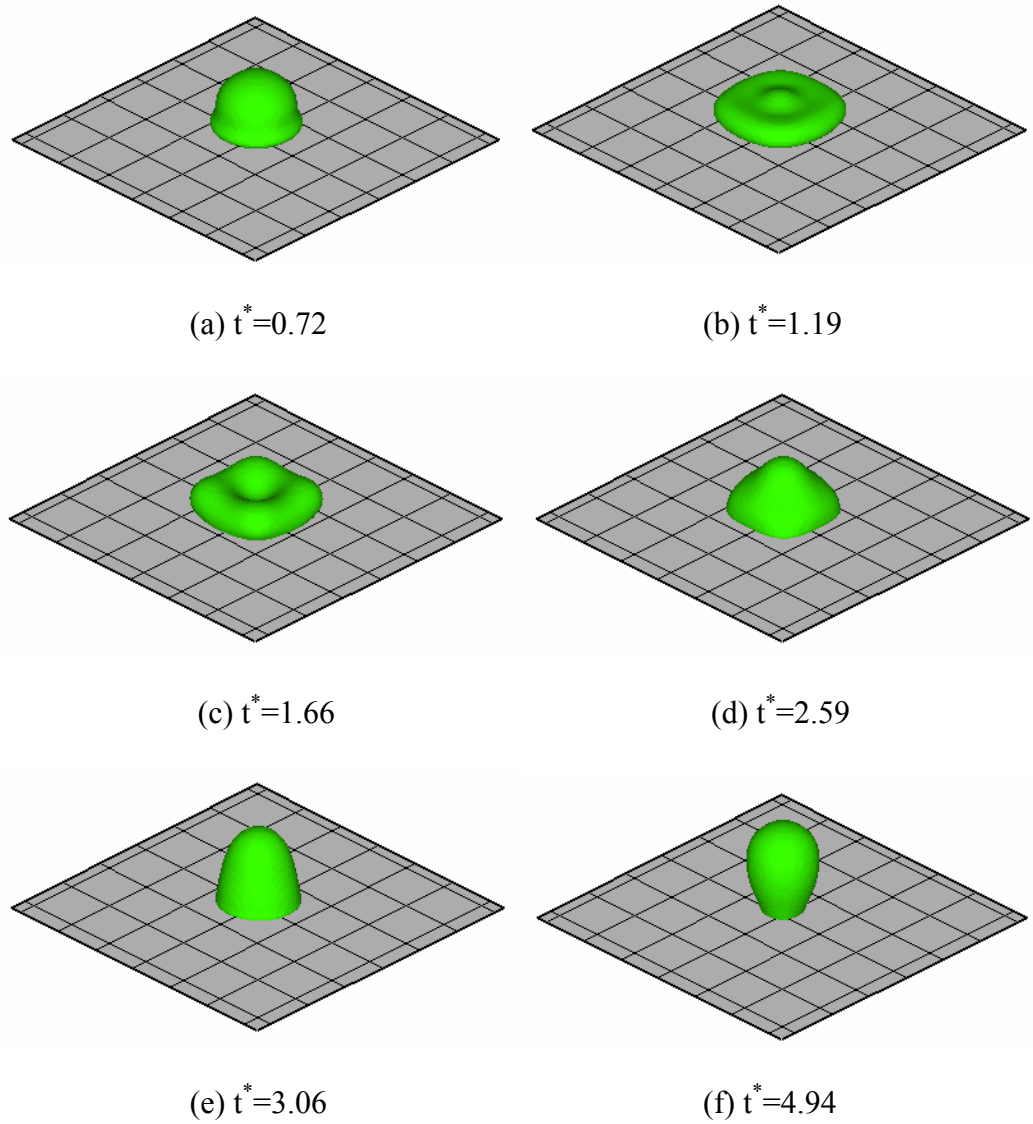

(a) t^*=0.72 (b) t^*=1.19

(c) t^*=1.66 (d) t^*=2.59

(e) t^*=3.06 (f) t^*=4.94

Figure 26: 3-D view of the time evolution of droplet shape for We=12.5, Re=1000.

5.5 Maximum spread factor analysis

According to mass conservation of the liquid film before and after impact:

$$\frac{\pi}{6}D^3 \approx \frac{\pi}{4}(Dd_{\max})^2 h \tag{5.3}$$

where $d_{\max}$ is the maximum spread factor, h is the height of the lamella when the droplet reaches its maximum spread factor. This yields:

$$d_{\max} \approx \sqrt{\frac{2D}{3h}} \tag{5.4}$$

Due to the diffusive nature of LBM (Lee & Lin (2005); Zheng et al. (2006)), the interface thickness between liquid and gas should not be any smaller than 2, otherwise the lamella might diffuse away. Since D=32 is used for all the simulation cases, and assuming h≥3, Eq. (5.4) reduces to $d_{\max} \le 2.67$. Thus, all the simulations conducted are properly chosen in order to meet this requirement on the maximum spread factor.

5.6 Parametric analysis on the maximum spread factor

In this section, three groups: the surface wettability, Weber number and Reynolds number, are studied separately to examine their influence on the liquid spreading behavior in the spreading phase.

In Figure 27, three different surfaces have been used: hydrophilic, neutral, and hydrophobic with static contact angles of θ_w=66.7°, θ_w=90°, θ_w=105°, respectively. As one can observe from the

figure, all the three curves behave similarly during most of the spreading phase. However, after $t^*=1$, some differences can be seen: on the hydrophilic surface, the droplet reaches a maximum spread factor of 2.45; on the neutral surface, the droplet reaches a maximum spread factor of 2.15; on the hydrophobic surface, the droplet reaches a maximum spread factor of 2.05. These results show that the surface wettability does have an influence on the maximum spread factor. Clearly, a spreading droplet tends to adhere to a hydrophilic surface while a hydrophobic surface tends to repel the spreading motion of the droplet.

In Figure 28, the influence of the drop inertia on the spreading of the lamella is shown, keeping the Weber number at a constant value of 36. Evidently, increasing the Reynolds number leads to an increase in the maximum spread factor. At Re=20, the maximum value for d^* is 1.5; at Re=100, $d^*_{max}=2.0$; at Re=200, $d^*_{max}=2.1$. From Re=20 to Re=100, the maximum spread factor increases by 33%, while from Re=100 to Re=200, the maximum spread factor only increases by 5%.

In Figure 29, the influence of the surface tension on the spreading process is compared by varying the Weber number while keeping the Reynolds number fixed at 200. As reported in an earlier study (Rioboo et al. (2002)), the influence of Weber number is weak, as can be seen from Figure 29. At We=36, $d^*_{max}=2.1$; at We=83, $d^*_{max}=2.2$.

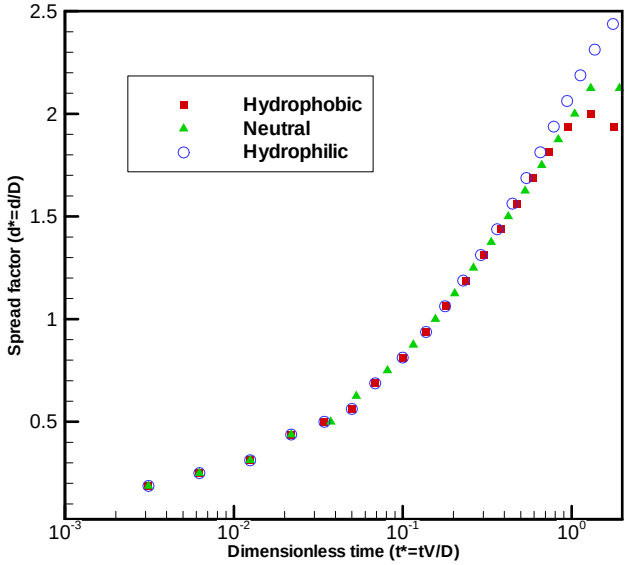

Figure 27: Wettability influence on the spreading behavior during spreading phase. (We=50, Oh=0.0071)

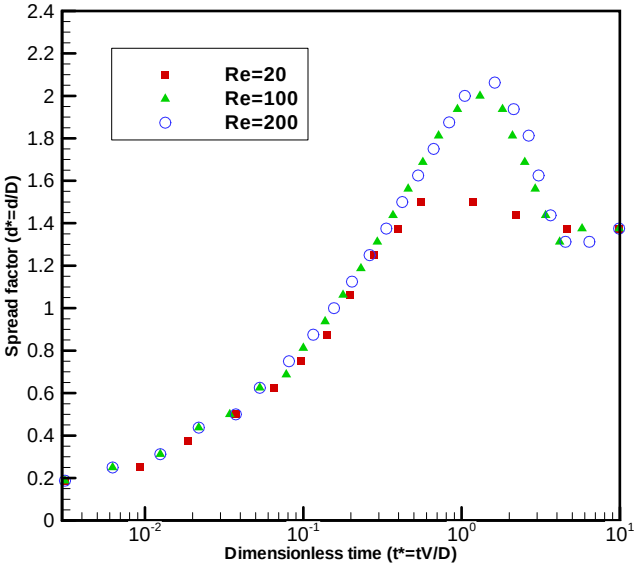

Figure 28: Reynolds number influence on the spreading behavior during spreading phase. (We=36 for all 3 cases)

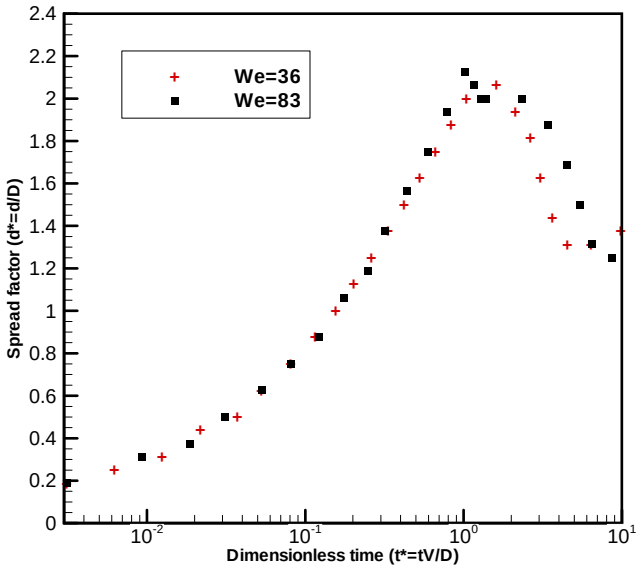

Figure 29: Weber number influence on the spreading behavior during spreading phase. (Re=200 for both cases)

5.7 Splashing break-up

In general, there are two possible outcomes of a droplet impingement on a solid dry surface, namely, deposition and splashing. Splashing is considered to be a more energetic pattern of impact outcome compared to deposition, as secondary droplets are ejected. Several experimental correlations have been proposed to quantify the deposition-splashing boundary. However, several questions remain unanswered and these correlations do no cover the entire range of governing parameters (Bussmann et al. (2000)). In this section, quantitative results of splashing will be presented. To the author's knowledge, such results of LBM or other numerical studies, have not been achieved or presented before. Since the quantitative results of splashing are computational intensive and they occur only for a certain combination of We and Re, limited

results are presented here. However, by invoking theoretical studies from the literature, it will be qualitatively shown at what point transition from deposition to splashing may occur.

One important and an easier starting point to look at the splashing problem is by the principle of mass and energy conservation before and after the impact (Mundo et al. (1995)):

$$E_k + E_p + E_s = E_k^{'} + E_p^{'} + E_s^{'} + E_d^{'},\ m = m^{'} \tag{5.5}$$

where E_k, E_p, E_s and E_d are the kinetic, potential, surface, dissipated energies respectively, and m and $m^{'}$ are the mass of the droplet before and after impact.

Thus, if $E_k + E_p + E_s > E_k^{'} + E_p^{'} + E_s^{'} + E_d^{'}$, it indicates that the energy before impact is not completely dissipated by the surface tension and viscous forces. This can lead to the formation of secondary droplets and splashing may occur.

The kinetic energy before impact can be written as:

$$E_k = \frac{1}{12}\Delta\rho V^2 \pi D^3 \tag{5.6}$$

where $\Delta\rho = \rho_L - \rho_G$, the density difference between liquid phase and gas phase.

The surface energy before impact can be written as:

$$E_s = \pi D\sigma \tag{5.7}$$

The surface energy after impact can be written as:

$$E_s^{'} = \frac{\pi}{4} d_{\max}^2 \sigma(1-\cos\theta) \tag{5.8}$$

where θ is the contact angle between the liquid-gas interface and solid when the lamella reached its maximum spreading diameter.

It is difficult to determine the dissipated energy because the velocity distribution inside the deforming droplet is not known. Chandra et al. (1991) used a very simple approximation to determine $E_d^{'}$:

$$E_d^{'} = \int_0^{t_d} \int_v \Phi * dv * dt \approx \Phi * v * t_d \tag{5.9}$$

where Φ is the dissipation per unit mass, and is given by:

$$\Phi = \mu(\frac{\partial u_x}{\partial y} + \frac{\partial u_y}{\partial x})\frac{\partial u_x}{\partial y} \approx \mu(\frac{V}{h})^2 \tag{5.10}$$

t_d is the time it takes for the drop to deform to a maximum, which is approximated by t_d=D/V. v is the volume of the lamella and is given by:

$$v \approx \frac{\pi}{4} d_{\max}^2 h \tag{5.11}$$

Combining Eqs. (5.5)-(5.11), and assuming E_p=E_p', we obtain a reduced form of Eq. (5.5) in terms of Weber number, Reynolds number and the maximum dimensionless spread factor,

$$\frac{3}{2}\frac{We}{\mathrm{Re}}(d_{\max}^*)^4 + (1-\cos\theta)(d_{\max}^*)^2 - (\frac{1}{3}\frac{\Delta\rho}{\rho_L}We + 4) = 0 \tag{5.12}$$

This could also be written in terms of Ohnesorge number as

$$Oh_c = \sqrt{\frac{3(1-\cos\theta)(d_{\max}^*)^2 - 12}{\frac{\Delta\rho}{\rho_L}\mathrm{Re}^2 - 4.5(d_{\max}^*)^4\,\mathrm{Re}}} \tag{5.13}$$

where Oh_c is the critical Ohnesorge number. For $\frac{\Delta\rho}{\rho_L} \sim 1$ at high density ratios, Eq (5.13) reduces to:

$$Oh_c = \sqrt{\frac{3(1-\cos\theta)(d^*_{\max})^2 - 12}{\mathrm{Re}^2 - 4.5(d^*_{\max})^4\,\mathrm{Re}}} \tag{5.14}$$

Eq (5.14) is the same equation proposed by Chandra et al. (1991).

Eq. (5.13) may determine the deposition-splashing boundary in terms of Reynolds number and the maximum spread factor. If the Ohnesorge number in the flow condition is larger than Oh_c, splashing will occur; otherwise, deposition will occur. However, Eqs (5.9)-(5.11) are very crude approximations for the dissipation energy, and the inaccuracy of these approximations may result in large uncertainty for predicting the outcomes. At the same time, an analysis of this kind qualitatively shows the effect of increasing the Reynolds and Weber number and their influence on splashing.

After Chandra's (1991) proposal of Oh_c, empirical correlations were proposed by several authors [Cossali et al. (1997); Mundo et al. (1995)], the demarcation between deposition and spreading of droplets can be determined based on the dimensionless value of K', defined as:

$$K' = We * Oh^{-0.4} \tag{5.15}$$

where K'= 650 is the deposition/splash threshold. When K'>650, splashing will occur; otherwise, deposition will occur.

Nine cases of LBM simulations are shown in Table 5, three of which resulted in splashing and one with partial rebound. The partial rebound case was reported earlier in Section 5.4. Table 5 also provides maximum spread factors at different Weber and Reynolds numbers, Ohnesorge

number for the simulation case, the critical Ohnesorge number from Eq. (5.13), the K' parameter from Eq. (5.15) maximum diameters from experimental correlations and finally the outcome of the particular case. According to the energy analysis and the correlation given in Eq. (5.15), when $Oh > Oh_c$, splashing should occur or when K'>650. The LBM outcome contradicts both criteria for some of the cases, suggesting further work in determining a suitable criterion for transition to splashing that covers a broad range of parameters. The current analysis or correlation is not accurate enough to be able to predict an outcome for the droplet impingement yet.

In Figure 30, two simulation results in the plane of $y=L_y/2$ are shown to compare deposition with splashing at the same Reynolds number of 200, but at different Ohnesorge numbers, Oh=0.03, Oh=0.046, respectively. These conditions are represented by Cases 6 and 7 in Table 5. The dynamic behavior of the droplets at different t* are given side by side for the two different Ohnesorge numbers. The three-dimensional view of the splashing in Case 7 is again shown in a different perspective in Figure 31. As seen in Table 5, for both cases 6 and 7, Oh_c is exceeded, yet splashing occurs only for Case 7. Similarly, the K' parameter for both cases does not exceed the deposition/splash threshold of 650 set by [Cossali et al. (1997); Mundo et al. (1995)] and therefore should not result in a splash, yet the outcome in each case is different.

Table 5: A list of simulation results with their outcomes and maximum spread factor

Case	Droplet Radius	We	Re	Oh	Oh_c (Eq.5.14)	K' (Eq.5.15)	d_{max}^{*LBM}	d_{max}^{**}	Outcome
1	16	50	1000	0.0071	0.0027	362.4	2.45	2.66	Deposition
2	16	500	50	0.447	0.067	690	1.88	1.96	Deposition
3	16	12.5	1000	0.0035	0.0019	120	2.25	2.37	Partial Rebound
4	16	36	20	0.3	0.307	58.3	1.5	1.35	Deposition
5	16	36	100	0.06	N/A	111	2.0	1.76	Deposition
6	16	36	200	0.03	0.0074	146.4	2.1	1.98	Deposition
7	16	83	200	0.046	0.012	286	2.2	2.12	Splashing
8	20	120	500	0.022	0.0024	553.3	2.1	2.54	Splashing
9	20	150	500	0.024	0.0036	661.4	2.2	2.59	Splashing

Notation:

d_{max}^{*LBM} : numerical value of maximum spread factor from LBM simulation

d_{max}^{**} : experimental correlation of maximum spread factor from Scheller et al. (1995)

Oh_c: calculated from Eq. (5.14)

K': calculated from Eq. (5.15)

Looking at the discrepancy between the correlation and the existing simulation, there are two major differences in the present numerical modeling of splash and the experiments on which the empirical correlation (Eq.5.15) is based. First, the density ratio of the liquid droplet to the

surrounding gas phase is fixed at 50 for the current simulations. This value is relatively small compared to the experimental data, which is in the range of 1000 for an air-water system at atmospheric pressure. This difference in density ratio translates to different values of the relative pressure between the simulations and experiments, with the relative pressure of the surrounding medium to be higher in the present LBM simulations as compared to that of experiments. No experiments have ever been reported regarding the influence of the ambient pressure on splashing, except one surprising discovery recently brought forward by Xu et al. (2005). They experimentally investigated the effect of the ambient pressure or the molecular weight of the surrounding gas on the splashing of droplets. Corona splash was the outcome when an alcohol drop was allowed to impinge on a dry surface at atmospheric pressure. However, when the pressure was reduced by a factor of 5, the corona completely disappeared and no splashing was observed. Thus, density (or pressure) of the surrounding gas may have a large influence on splashing and may be the cause of the discrepancy in the threshold set by the correlation. Thus, the mechanism of this kind of influence warrants further study. Secondly, the surface roughness and the uncertainty in the experiments are also factors in splashing. These influences are not reproduced in the current LBM simulations, since the surface of impact is considered to be ideally smooth and the simulation conditions are isotropic. Since we have validated the LBM results both for single- and two-phase flows, and the theory and empirical correlation do not match, we conclude that there needs to be more work done in this area to obtain a correlation that not only includes a broad range of existing parameters but also a combination of these parameters.

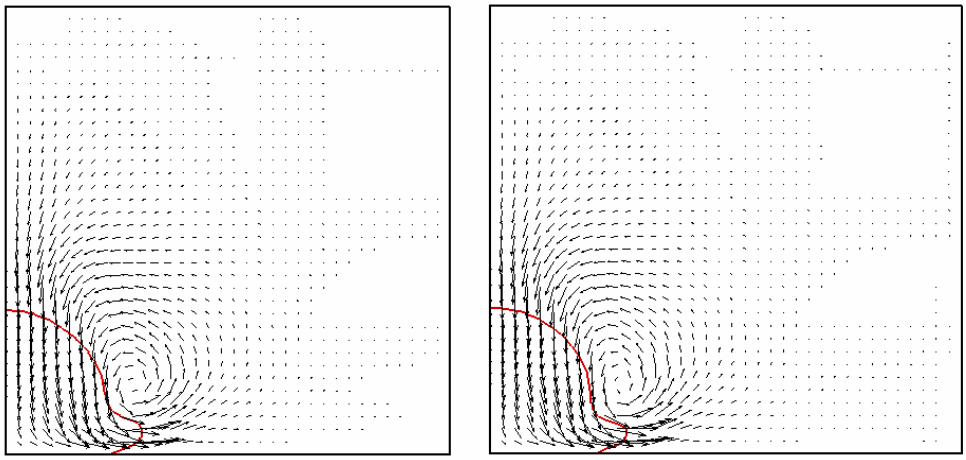

(a) t*=0.47

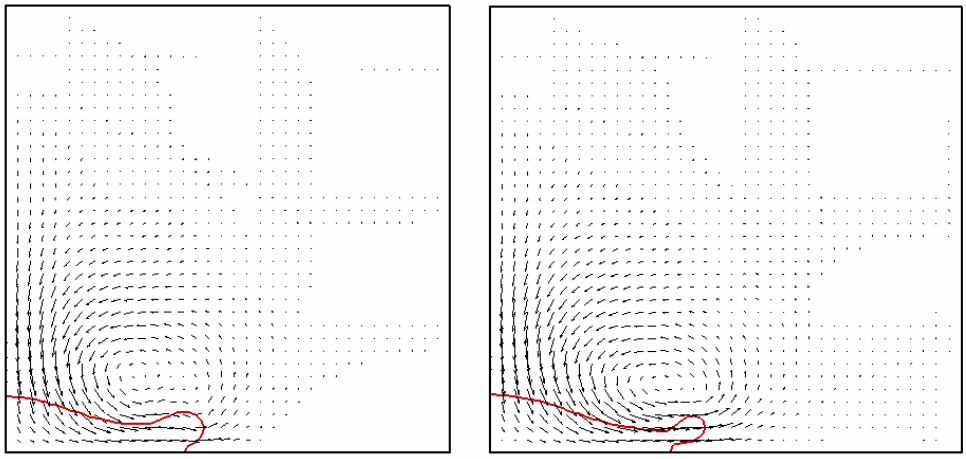

(b) t*=1.1

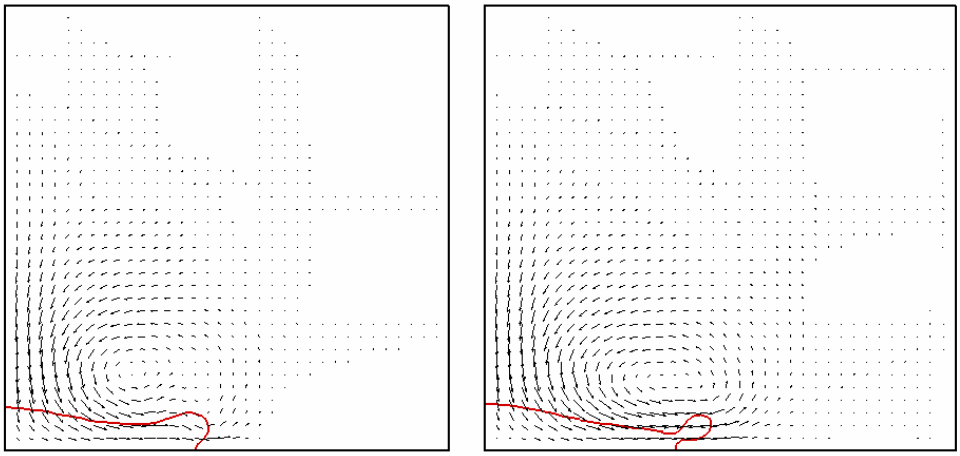

(c) t*=1.25

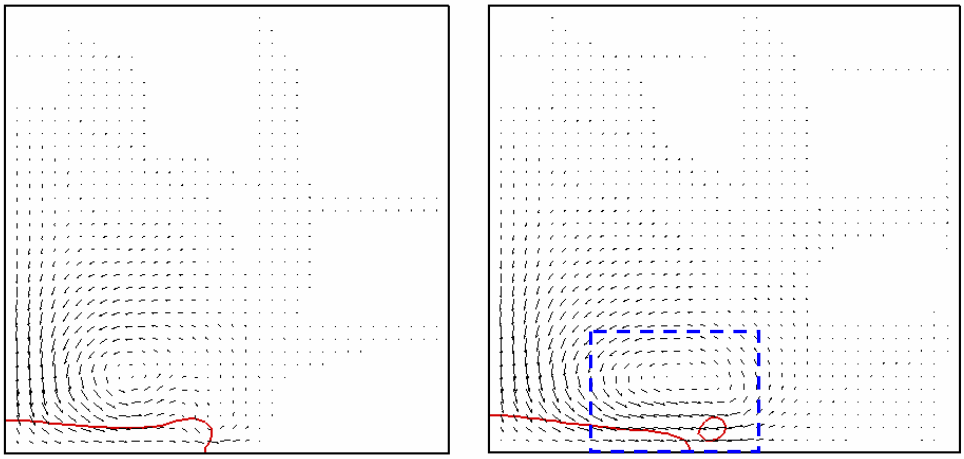

(d) t*=1.41

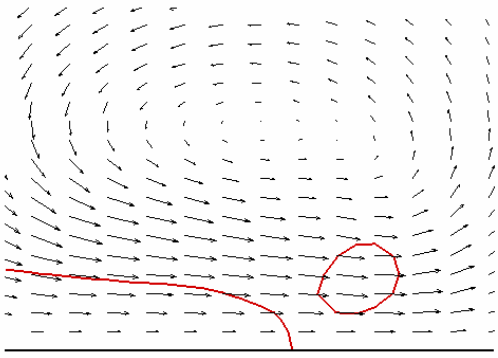

(e) same as (d) for Oh=0.046 zoomed in

Figure 30: Comparison between deposition and splashing break-up (We=36 on the left for Oh=0.03 and We=83 on the right for Oh=0.046, both at Re=200)

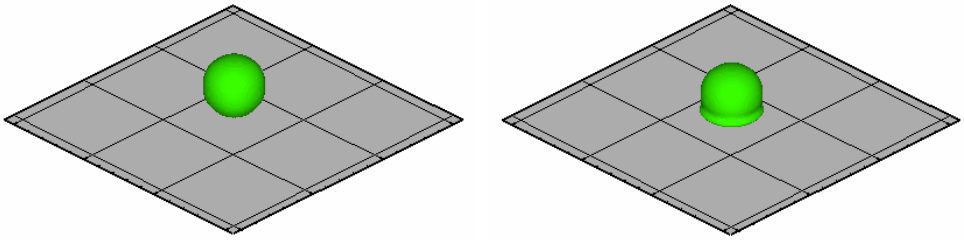

(a) t*=0 (b) t*=0.16

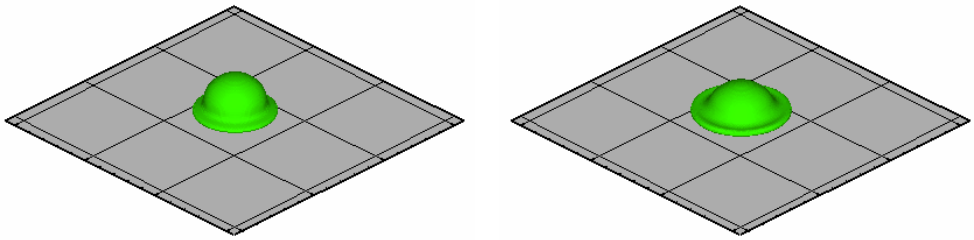

(c) t*=0.31 (d) t*=0.47

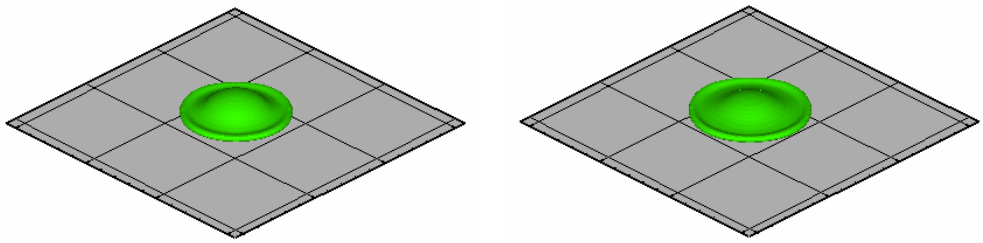

(e) t*=0.63 (f) t*=0.78

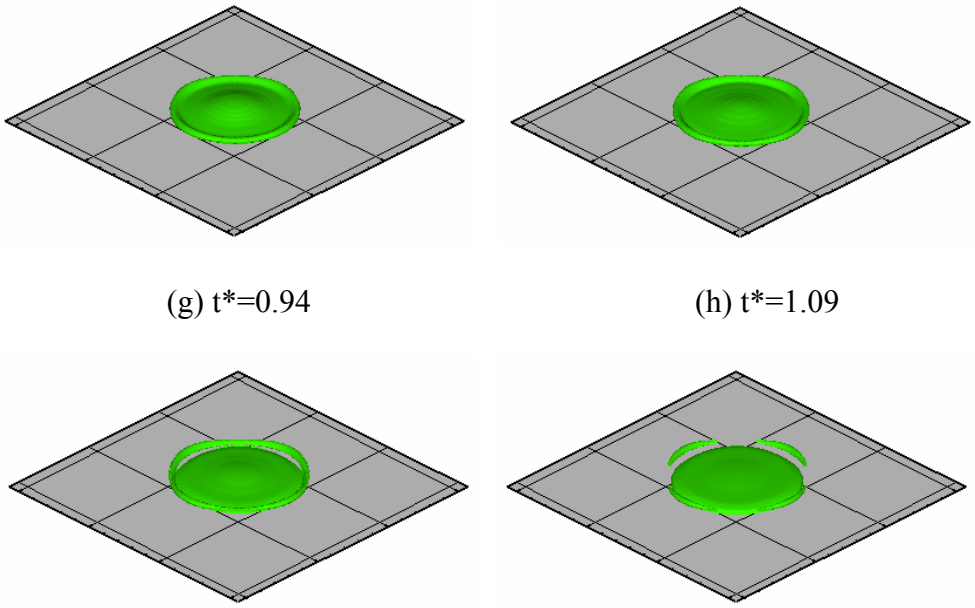

(g) t*=0.94 (h) t*=1.09

(i) t*=1.25 (j) t*=1.41

Figure 31: Three-dimensional simulation results to show splashing break-up after the droplet reaches its maximum spread factor (We=83, Oh=0.046)

CHAPTER SIX: CONCLUSIONS AND FUTURE STUDIES

In this work, a Lattice Boltzmann method is presented to simulate droplet collision and droplet impact at a relatively large density ratio of 50 in a three-dimensional Cartesian system. This density ratio, although much smaller than that for air-water, is still high compared to what the other LBM methods have been able to achieve. The current method has its benefits, considering the numerical instability which arises when dealing with large density ratios in LBM (Gunstensen et al. (1991); Shan & Chen (1993); Swift et al. (1995); He et al. (1999)). The surface wettability is suitably incorporated by a novel boundary treatment. Hydrophilic, neutral and hydrophobic surfaces have been successfully simulated to study the role of surface wetting characteristics in droplet impingement problems.

It is shown that during the early stage of impact, the spread factor is proportional to a power of dimensionless time, given by: $d^*_{max}=2.5t^{*0.5}$. It compares well with the theoretical analysis and existing experimental correlations (Rioboo et al. (2002)). In the spreading phase, it is shown that the maximum spread factor increases with an increase in Reynolds number and Weber number, with the Reynolds number registering a higher influence. In addition, maximum spread factors are found to increase in the ascending order when compared to hydrophobic, neutral and hydrophilic surfaces.

Two different outcomes of impingement have been shown: deposition and splashing. Splashing occurs at a higher Reynolds number and Ohnesorge number compared to deposition. The transition to splashing is qualitatively studied by a simple energy analysis. Since the density or pressure of the surrounding gas phase also plays a key role in determining the deposition-splashing threshold, it is shown that the threshold of the present simulation results is lower than the experimental data. Although the effect of pressure needs further study, it appears that splashing can be avoided by reducing the system pressure.

LIST OF REFERENCES

Asai, A., Shioya, M., Hirasawa, S., and Okazaki, T., "Impact of an ink drop on paper", The Journal of Imaging Science and Technology, 37, 205-207 (1993)

Bergeron, V., Bonn, D., Martin, J.Y., and Vovelle, L., "Controlling droplet deposition with polymer additives", Nature, 405, 772-775 (2000)

Briant, A.J., Wagner, A.J., Yeomans, J.M., "Lattice Boltzmann simulations of contact line motion. I.Liquid-gas system", Physical Review E, 69, 031602-031616 (2004)

Bussmann, M., Chandra, S., and Mostaghimi, J., "Modeling the splash of a droplet impacting a solid surface", Physics of Fluids, 12, 3121-3132 (2000)

Chandra, S., and Avedisian, C.T., "On the collision of a droplet with a solid surface", Proc. R. Soc. Lond. A, 432, 13-41 (1991)

Chen, S., and Doolen, G..D., "Lattice Boltzmann method for fluid flows", Annual Review of Fluid Mechanics, 30, 329-364 (1998)

Chen, S., Martinez, D., and Mei, R., "On boundary conditions in lattice Boltzmann methods", Physics of Fluids, 8, 2527-2536 (1996)

Crooks, R., Cooper-Whitez, J., and Boger, D.V., "The role of dynamic surface tension and elasticity on the dynamics of drop impact", Chemical Engineering Science, 56, 5575-5592 (2001)

Engel, O.G., "Waterdrop collisions with solid surfaces", Journal of Research of the National Bureau of Standards, 54, 281-295 (1955)

Cossali, G.E., Coghe, A. and Marengo, M., "The impact of a single drop on a wetted solid surface", Experiments in Fluids, 22, 463-472 (1997)

Ford, R. E., and Furmidge, C.G.L, "Impact and spreading of spray drops on foliar surfaces, wetting", Society of Chemical Industry, Monnograph, 417-432 (1967)

Frisch, U., Hasslacher, B., Pomeau, Y., "Lattice-gas automata for the Navier-Stokes equations", Physical Review Letters, 56, 1505-1508 (1986)

Frohn, A., and Roth, N., "Dynamics of droplets", Springer, Berlin (2000)

Fukai, J., Shiiba, Y., Yamamoto, T., Miyataka, O., Poulikakos, D., Megaridis, C.M., and Zhao. Z., "Wetting effects on the spreading of a liquid droplet colliding with a flat surface: experiment and modeling", Physics of Fluids, 7, 236-247 (1995)

Fukai, J., Zhao, Z., Poulikakos, D., Megaridis, C.M., and Miyatake, O., "Modeling of the deformation of a liquid droplet impinging upon a flat surface", Physics of Fluids A, 5, 2588-2599 (1993)

Glimm, J., Grove, J.W., Li, X.L., Shyue, K., Zeng, Y., and Zhang, Q., "Three dimensional front tracking", SIAM Journal on Scientific Computing, 19, 703-727 (1998)

Grunau, D., Chen, S., and Egger, K., "A lattice Boltzmann model for multi-phase fluid flows", Physics of Fluids A: Fluid Dynamics, 5, 2557-2562 (1993)

Gunstensen, A.K., Rothman, D.H., Zaleski, S., Zanetti, G., "Lattice Boltzmann model of immiscible fluids", Physical Review A, 43, 4320–4327 (1991)

Gupta, A., Kumar, R., "Simulation of droplet flows using Lattice Boltzmann method", Proceedings of the Sixth International ASME Conference on Nanochannels, Microchannels and Minichannels, Darmstadt, Germany, (2008)

Haler, K.K., Ventikos, Y., Poulikakos, D., and Monkewitz, P., “Computational study of high-speed liquid droplet impact”, Journal of Applied Physics, 92, 2821-2828 (2002)

Hardy, J., de Pazzis, O., and Pomeau, Y., “Molecular dynamics of a classical lattice gas: Transport properties and time correction functions”, Physical Review A, 13, 1949-1961 (1976)

Harlow, F.H., and Shannon, J.P., “The splash of a liquid drop”, Journal of Applied Physics, 38, 3855-3866 (1967)

Harlow, F.H., and Welch, J.E., “Numerical calculation of time-dependent viscous incompressible flow of fluid with free surface”, Physics of Fluids, 8, 2182-2189 (1965)

He, X., and Luo, L.S., “Theory of the lattice Boltzmann method: From the Boltzmann equation to the lattice Boltzmann equation”, Physical Review E, 56, 6811-6817 (1997)

He, X., Shan, X., and Doolen, G., “Discrete Boltzmann equation model for nonideal gases”, Physical Review E, 57, R13-R16 (1998)

He, X., Chen, S., Zhang, R., “A lattice Boltzmann scheme for incompressible multiphase flow and its application in simulation of Rayleigh–Taylor instability”, Journal of Computational Physics, 152, 642–663 (1999)

Hirt, C.W., and Nichols, B.D., "Volume of fluid (VOF) method for the dynamics of free boundaries", Journal of Computational Physics, 39, 201-225 (1981)

Hou, S., Zou, Q., Doolen, G., and Cogley, A., “Simulation of cavity flow by the lattice Boltzmann method”, Journal of Computational Physics, 118, 329-347 (1995)

Huang, Y.C., Hammitt, F.G., and Yang, W.J., ‘‘Hydrodynamic phenomena during high-speed collision between liquid droplet and rigid plane,’’ Transactions of the ASME, Journal of Fluids Engineering, 276–294 (1973)

Inamuro, T., Konishi, N., Ogino, F., “A Galilean invariant model of the lattice Boltzmann method for multiphase fluid flows using free-energy approach”, Computer Physics Communications, 129, 32-45 (2000)

Inamuro, T., Ogata, T., Tajima, S., and Konishi, N., “A lattice Boltzmann method for incompressible two-phase flows with large density differences”, Journal of Computational Physics, 198, 628-644 (2004)

Inamuro, T., Tajima, S., and Ogino, F., “Lattice Boltzmann simulation of droplet collision dynamics”, International Journal of Heat and Mass Transfer, 47, 4649-4657 (2004)

Kang, Q., Zhang, D., Chen, S., “Displacement of a three-dimensional immiscible droplet in a duct”, Journal of Fluid Mechanics, 545, 41-66 (2005)

Kim, H.Y., and Chun, J.H., “The recoiling of liquid droplets upon collision with solid surfaces”, Physics of fluids, 13, 643-659 (2001)

Kim, H., Park, S., and Min, K., “Imaging the high-speed impact of microdrop on solid surface”, Review of scientific instruments, 74, 4930-4937 (2003)

Lee, T., and Lin, C.-L., “A stable discretization of the lattice Boltzmann equation for simulation of incompressible two-phase flows at high density ratio”, Journal of Computational Physics, 206, 16-47 (2005)

Mao, T., Kuhn, D.C.S., and Tran H., “Spread and rebound of liquid droplets upon impact on flat surfaces”, AIChE Journal, 43, 2169-2179 (1997)

McCracken, M., “Development and evaluation of lattice Boltzmann models for investigation of liquid break-up”, Ph.D. thesis (2004)

McNamara, G.R., and Zanetti, G., “Use of Boltzmann equation to simulate lattice automata”, Physical Review Letters, 61, 2332-2335 (1988)

Mo, G.C.H., Liu, W., and Kwok, D.Y., “Surface-Ascension of Discrete Liquid Drops via Experimental Reactive Wetting and Lattice Boltzmann Simulation”, Langmuir, 21, 5777-5782 (2005)

Mourrougou-Candoni, N., Prunet-Foch, B., Legay, F., and Vignes-Adler, M., “Retraction Phenomena of Surfactant Solution Drops upon Impact on a Solid Substrate of Low Surface Energy”, Langmuir, 15, 6563-6574 (1999)

Mukherjee, S., “Numerical simulation of wall impinging drops”, Ph.D. thesis (2006)

Mukherjee, S., and Abraham, J., “Investigations of drop impact on dry walls with a lattice-Boltzmann model”, Journal of Colloid and Interface Science, 312, 341-354 (2007)

Mundo, CHR., Sommerfeld, M., and Tropea, C., “Droplet-wall collisions: Experimental studies of the deformation and breakup process”, International Journal of Multiphase Flow, 21, 151-173 (1995)

Noh, W., and Woodward, P., “SLIC (simple line interface calculation)”, Proc. 5th Int. Conf. Fluid Dyn., 59, 330–340 (1976)

Ok, H., “Particle-Laden drop impingement on a sold surface”, Ph.D. thesis (2005)

Osher, S., and Sethian, J., “Fronts propagating with curvature-dependent speed: Algoriths based on Hamilton-Jacobi formulations”, Journal of Computational Physics, 79, 12-49 (1988)

Park, H., Carr, W.W., Zhu, J., and Morris, J.F., "Single drop impaction on a solid surface", AIChE Journal, 49, 2461-2471 (2003)

Pasandideh-Fard, M., Qiao, Y.M., Chandra, S., and Mostaghimi, J., "Capillary effects during droplet impact on a solid surface", Physics of Fluids, 8, 650-659 (1996)

Qian, J., D.d'Humieres, and Lallemand, P., "Lattice BGK models for Navier-Stokes equations", Europhysics Letters, 17, 479-484 (1992)

Rider, W.J., and Kothe, D.B., "Reconstructing volume tracking", Journal of Computational Physics, 141, 112–152 (1998)

Richard D., Clanet, C., and Quéré, D., "Contact time of a bouncing drop", Nature, 417, 811 (2002)

Rioboo, R., Marengo, M., and Tropea, C., "Outcomes from a drop impact on solid surfaces", Atomization and Sprays, 11, 155-164 (2001)

Rioboo, R., Marengo, M., and Tropea, C., "Time evolution of liquid drop impact onto solid, dry surfaces, Experiments in fluids", 33, 112-124 (2002)

Rothman, D.H., and Keller, J.M., "Immiscible cellular-automaton fluids", Journal of Statistical Physics, 52, 1119-1127 (1988)

Sankaranarayanan, K., Shan, X., Kevrekidis, I.G., and Sundaresan, S., "Bubble flow simulation with the lattice Boltzmann method", Chemical Engineering Science, 54, 4817-4823 (1999)

Sankaranarayanan, K., Shan, X., Kevrekidis, I.G., and Sundaresan, S., "Analysis of drag and virtual mass forces in bubbly suspensions using an implicit formulation of the lattice Boltzmann method", Journal of Fluid Mechanics, 452, 61-96 (2002)

Sethian, J.A., and Smereka, P., “Level set methods for fluid interfaces”, Annual Review of Fluid Mechanics, 35, 341-372 (2003)

Scheller, B.L., and Bousfield, D.W., “Newtonian drop impact with solid surface”, AIChE Journal, 41(6), 1357-1367 (1995)

Shan, X., and Chen, H., “Lattice Boltzmann model for simulating flows with multiple phases and components”, Physical Review E, 47, 1815–1819 (1993)

Shan, X., and Doolen, G..D., “Multicomponent lattice-Boltzmann model with interparticle interaction”, Journal of Statistical Physics, 81, 379-393 (1995)

Sikalo, S., Marengo, M., Tropea, C., and Ganic, E., “Analysis of impact of droplets on horizontal sufaces”, Experimental thermal and fluid science, 25, 503-510 (2002)

Swift, M.R., Osborn, W.R., and Yeomans, J.M., “Lattice Boltzmann simulation of nonideal fluids”, Physical Review Letters, 75, 830–833 (1995)

Swift, M.R., Orlandi, E., Osborn, W.R., and Yeomans, J.M., “Lattice Boltzmann simulations of liquid-gas and binary fluid systems”, Physical Review E, 54, 5041-5052 (1996)

Thoroddsen, S.T. and Sakakibara, J., “Evolution of the fingering pattern of an impacting drop”, Physics of Fluids, 10, 1359-1374 (1998)

Trapaga, G.., and Szekely, J., “Mathematical modeling of the isothermal impingement of liquid droplets in spray processes,” Metallurgical and Materials Transactions B, 22, 901-914 (1991)

Tsurutani, K, Yao, M., Senda, J., and Fujimoto, J., “Numerical analysis of the deformation process of a droplet impinging upon a wall”, JSME International Journal Series II, 33, 555-561 (1990)

Wolf-Gladrow, D., “Lattice-Gas Cellular Automata and Lattice Boltzmann Models”, Lecture Notes in mathematics, No. 1725. Springer, Berlin (2000)

Worthington, A.M., “On the forms assumed by drops of liquids falling vertically on horizontal plate”, Proc. R. Soc. Lond., 25, 261-272 (1876)

Xu, L., Zhang, .W.W., Nagel, S.R., “Drop splashing on a dry smooth surface”, Physical Review Letters, 94, 184505.1-184505.4 (2005)

Yarin, A.L., “Drop Impact Dynamics: Splashing, Spreading, Receding, Bouncing…”, Annual Review of Fluid Mechanics, 38, 159-192 (2006)

Yuan, P., Laura, S., “Equation of state in a lattice Boltzmann model”, Physics of Fluids, 18, 042101.1-042101.11 (2006)

Zhang, X., and Basaran, O.A., “Dynamic surface tension effects in impact of a drop with a solid surface, Journal of colloid and interface science”, 187, 166-178 (1997)

Ziegler, D.P., “Boundary conditions for lattice Boltzmann simulations”, Journal of Statistical Physics, 71, 1171-1177 (1993)